

Satellite Metallicity Enhancement I: Suppressed Star Formation, Stellar Mass Loss, and Enriched Inflow of DESI and EAGLE Galaxies around Massive Clusters

YUANYE LIN,^{1,2} YING ZU,^{1,2} J. AGUILAR,³ S. AHLEN,⁴ D. BROOKS,⁵ T. CLAYBAUGH,³ A. CUCEU,³ A. DE LA MACORRA,⁶ A. FONT-RIBERA,^{7,8} J. E. FORERO-ROMERO,^{9,10} SATYA GONTCHO A GONTCHO,¹¹ G. GUTIERREZ,¹² R. JOYCE,¹³ M. LANDRIAU,³ L. LE GUILLOU,¹⁴ A. MEISNER,¹³ R. MIQUEL,^{7,8} J. MOUSTAKAS,¹⁵ W. J. PERCIVAL,^{16,17,18} F. PRADA,¹⁹ I. PÉREZ-RÀFOLS,²⁰ G. ROSSI,²¹ E. SANCHEZ,²² D. SCHLEGEL,³ J. SILBER,³ D. SPRAYBERRY,¹³ G. TARLÉ,²³ B. A. WEAVER,¹³ AND H. ZOU²⁴

¹State Key Laboratory of Dark Matter Physics & Tsung-Dao Lee Institute, Shanghai Jiao Tong University, Shanghai, 200240, China.

²Department of Astronomy, School of Physics and Astronomy, Shanghai Jiao Tong University, Shanghai 200240, China

³Lawrence Berkeley National Laboratory, 1 Cyclotron Road, Berkeley, CA 94720, USA

⁴Department of Physics, Boston University, 590 Commonwealth Avenue, Boston, MA 02215 USA

⁵Department of Physics & Astronomy, University College London, Gower Street, London, WC1E 6BT, UK

⁶Instituto de Física, Universidad Nacional Autónoma de México, Circuito de la Investigación Científica, Ciudad Universitaria, Cd. de México C. P. 04510, México

⁷Institució Catalana de Recerca i Estudis Avançats, Passeig de Lluís Companys, 23, 08010 Barcelona, Spain

⁸Institut de Física d'Altes Energies (IFAE), The Barcelona Institute of Science and Technology, Edifici Cn, Campus UAB, 08193, Bellaterra (Barcelona), Spain

⁹Departamento de Física, Universidad de los Andes, Cra. 1 No. 18A-10, Edificio Ip, CP 111711, Bogotá, Colombia

¹⁰Observatorio Astronómico, Universidad de los Andes, Cra. 1 No. 18A-10, Edificio H, CP 111711 Bogotá, Colombia

¹¹University of Virginia, Department of Astronomy, Charlottesville, VA 22904, USA

¹²Fermi National Accelerator Laboratory, PO Box 500, Batavia, IL 60510, USA

¹³NSF NOIRLab, 950 N. Cherry Ave., Tucson, AZ 85719, USA

¹⁴Sorbonne Université, CNRS/IN2P3, Laboratoire de Physique Nucléaire et de Hautes Energies (LPNHE), FR-75005 Paris, France

¹⁵Department of Physics and Astronomy, Siena University, 515 Loudon Road, Loudonville, NY 12211, USA

¹⁶Department of Physics and Astronomy, University of Waterloo, 200 University Ave W, Waterloo, ON N2L 3G1, Canada

¹⁷Perimeter Institute for Theoretical Physics, 31 Caroline St. North, Waterloo, ON N2L 2Y5, Canada

¹⁸Waterloo Centre for Astrophysics, University of Waterloo, 200 University Ave W, Waterloo, ON N2L 3G1, Canada

¹⁹Instituto de Astrofísica de Andalucía (CSIC), Glorieta de la Astronomía, s/n, E-18008 Granada, Spain

²⁰Departament de Física, EEBE, Universitat Politècnica de Catalunya, c/Eduard Maristany 10, 08930 Barcelona, Spain

²¹Department of Physics and Astronomy, Sejong University, 209 Neungdong-ro, Gwangjin-gu, Seoul 05006, Republic of Korea

²²CIEMAT, Avenida Complutense 40, E-28040 Madrid, Spain

²³University of Michigan, 500 S. State Street, Ann Arbor, MI 48109, USA

²⁴National Astronomical Observatories, Chinese Academy of Sciences, A20 Datun Road, Chaoyang District, Beijing, 100101, P. R. China

ABSTRACT

Environmental effects are a primary driver of elevated gas-phase metallicities in galaxies around massive clusters, but the underlying physical mechanisms for this satellite metallicity enhancement (SME) are still unclear. Using the Dark Energy Spectroscopic Instrument (DESI) Data Release 1, we present the first measurement of the average SME as a function of projected cluster-centric distance. The resulting profile reveals three distinct regimes: a steep decline from the cluster center, a plateau near the cluster boundary, and an extended downturn across several cluster radii. Remarkably, the complex shape and amplitude of this observed SME profile are successfully reproduced in the EAGLE cosmological simulation. Drawing insights from EAGLE, we develop a novel satellite chemical evolution model to decompose the observed SME into physical contributions from suppressed star formation, stellar mass loss, and enriched gas inflow. Our analysis shows that continuous accretion of enriched intracluster medium dominates the SME plateau within the cluster virial radius, while mass loss and quenching jointly drive the rapid metallicity decline in the cluster core. Our method disentangles the impacts of three environmental processes on galactic chemical enrichment in the cosmic web, providing

a powerful framework for understanding cluster galaxy evolution with current and future spectroscopic surveys.

Keywords: Galaxies (573) — Interstellar medium (847)

1. INTRODUCTION

Galaxies in the cluster environment exhibit higher metallicity in their interstellar medium (ISM) compared to those in the field (G. A. Shields et al. 1991; E. D. Skillman et al. 1996; M. Mouhcine et al. 2007; A. Pasquali et al. 2012; Y.-j. Peng & R. Maiolino 2014). This satellite metallicity enhancement (SME) provides a unique probe into the key environmental processes that expedite the dynamical and chemical evolution of galaxies (A. Boselli & G. Gavazzi 2006; M. R. Blanton & J. Moustakas 2009; Y. Peng et al. 2015). In this paper, we measure the SME profile as a function of distance from massive clusters using galaxies from the Dark Energy Spectroscopic Instrument (DESI; M. Levi et al. 2013; DESI Collaboration et al. 2016a,b) survey Data Release 1 (DR1; DESI Collaboration et al. 2025) and compare it to the prediction by the EAGLE simulation (J. Schaye et al. 2015; R. A. Crain et al. 2015), in hopes of developing a physically-motivated model of chemical enrichment for galaxies at the nexus of the cosmic web.

The ISM metallicity is commonly defined as $Z_{\text{ISM}} \equiv 12 + \log(\text{O}/\text{H})$, where O/H indicates the oxygen-to-hydrogen abundance ratio in the ISM. The observed Z_{ISM} is primarily correlated with the stellar mass M_* of galaxies, yielding the well-established “mass-metallicity relation” (MZR; J. Lequeux et al. 1979; C. A. Tremonti et al. 2004; S. Savaglio et al. 2005; D. K. Erb et al. 2006; F. Mannucci et al. 2009; B. H. Andrews & P. Martini 2013; R. L. Sanders et al. 2021; M. Curti et al. 2023). Additionally, the observed scatter of Z_{ISM} about the median MZR is correlated with the star formation rate (SFR), resulting in a $Z_{\text{ISM}}-M_*-\text{SFR}$ relation that does not evolve at least up to $z \sim 3$ (a.k.a., fundamental metallicity relation or FMR; F. Mannucci et al. 2010; M. A. Lara-López et al. 2010; M. W. Topping et al. 2021).

In traditional gas-regulator models, the FMR is interpreted as a consequence of instantaneous chemical equilibrium between gas accretion and consumption (N. Bouché et al. 2010; R. Davé et al. 2012; S. J. Lilly et al. 2013). Challenging this view, Y. Lin & Y. Zu 2023 (hereafter referred to as LZ23) demonstrated that an FMR naturally emerges from the non-equilibrium chemical evolution of galaxies in both the EAGLE simulation and the Sloan Digital Sky Survey (SDSS; D. G. York et al. 2000). They developed a non-equilibrium chem-

ical evolution model (NE-CEM) that can explicitly reconstruct the average histories of star formation (SF), mass-loading, and gas accretion as functions of time for field galaxies at any observed M_* and SFR. A key finding of LZ23 is that although galaxies spent most of their history out of chemical equilibrium, the self-similarity of their evolutionary histories produces a consistent FMR up to $z=3$. Consequently, the ISM metallicity of a typical star-forming galaxy in the field environment can be quantitatively understood within the NE-CEM framework.

However, after the star-forming galaxy falls into a massive cluster, it will likely experience the so-called “delayed-then-rapid” quenching process (A. R. Wetzel et al. 2013), sustaining as a star-forming satellite for 2–4 Gyr before a rapid transition onto the red-sequence (due to e.g., an increased ram pressure stripping in the cluster core; C. Maier et al. 2019). During the “delayed” phase, this satellite galaxy will experience stellar mass loss from the strong tidal field (J. E. Taylor & A. Babul 2004; S. B. Green et al. 2021) and suppressed SF due to strangulation (R. B. Larson et al. 1980; Y. Peng et al. 2015), while still accreting residual gas from the metal-rich intracluster medium (ICM; S. Schindler et al. 2005; A. Gupta et al. 2018). As a result, the satellite metallicities will systematically deviate from those of isolated field galaxies at the same *observed* M_* and SFR. In this work, we present the first measurement of the scale-dependent SME profile for cluster galaxies using the DESI DR1 data, establishing a benchmark to evaluate subgrid physics in cosmological hydrodynamic simulations like EAGLE.

In theory, the scale-dependence of the SME profile is shaped by the combined environmental effects of mass loss, SF suppression, and enriched inflow at different radii away from the massive clusters. In particular, mass loss primarily reduces M_* without changing the metallicity in the central region — the quantity directly measured by fiber-fed spectrographs like DESI. Meanwhile, suppressed SF modifies the chemical enrichment history (CEH) of a galaxy by modulating the metal production vs. wind ejection (Y. Lin & Y. Zu 2023), and an enriched gas inflow directly elevates the metallicity of the ISM compared to the field galaxies where the accreted gas is typically chemically pristine (K. Finlator & R. Davé 2008; A. M. Brooks et al. 2009). While prior

observational studies have provided qualitative assessments of the individual impacts of those processes on the SME (S. L. Ellison et al. 2009; V. Petropoulou et al. 2011; D. Williamson et al. 2016; D. Sotillo-Ramos et al. 2021), a rigorous understanding of the SME profile as a function of cluster-centric radius is still lacking. In this paper, we will draw analytic insights from the EAGLE simulation and build a simple yet comprehensive CEM for the satellite galaxies in DESI. Based on the NE-CEM developed by LZ23, our novel method aims to explicitly reconstruct the satellite histories of mass-loss, SF, and gas accretion inside the cluster, in order to accurately disentangle their contributions to the observed SME profile.

This is the first in a series of three papers that will systematically explore the SME physics using DESI DR1. The methodology presented in this paper will serve as the foundation for interpreting our more comprehensive DESI SME measurements in papers II and III.

We organize this paper as follows. We measure the overall SME profiles from DESI DR1 and EAGLE in §2 and develop a satellite NE-CEM in §3. In §4, we describe our method for identifying the physical processes that contribute to SME. From analyzing the EAGLE simulation data, we decompose the observed SME profile into three distinct contributions in §5. We summarize our results and look to the future in §6. We adopt a flat Λ CDM cosmology with $\Omega_m=0.315$ and $h=0.674$ (Planck Collaboration et al. 2020) to calculate the distances for the DESI measurements.

2. SATELLITE METALLICITY ENHANCEMENT IN DESI AND EAGLE

As a first-cut analysis in this paper, we measure the overall SME profile of all star-forming galaxies in DESI DR1 surrounding clusters with $M_h > 10^{12} h^{-1} M_\odot$ from the DESI halo-based cluster catalog. We defer a more comprehensive suite of SME measurements to the upcoming paper II, which will reveal the complex dependence of SME profile on stellar mass, SFR, and halo mass. We describe the data and measurement method in §2.1 and 2.2, but the impatient readers can skip these two subsections to §2.3, where we compare the measured SME profiles between DESI and EAGLE.

2.1. Galaxy and Cluster Samples in DESI DR1

2.1.1. The DESI Star-forming Galaxy Sample

DESI is a prominent Stage-IV dark energy survey conducted with the 4-meter Mayall telescope at Kitt Peak (M. Levi et al. 2013; DESI Collaboration et al. 2016a,b, 2022, 2024a,b). The DESI instrument obtains simultaneous spectra of almost 5000 objects (J. Guy

et al. 2023; C. Poppett et al. 2024; E. F. Schlafly et al. 2023). Our analysis is based on the Bright Galaxy Survey (BGS) component of DESI DR1 (DESI Collaboration et al. 2025; A. G. Adame et al. 2025). This component includes the spectra of 6,280,198 objects from the BGS Main Survey and 385,837 from the Survey Validation (SV; C. Hahn et al. 2023), covering a redshift range of $0 < z < 0.6$. The BGS Main Survey consists of the BGS Bright sample ($r < 19.5$) and BGS Faint sample ($19.5 < r < 20.175$), reaching galaxies > 2 mag fainter than the Sloan Digital Sky Survey (SDSS; D. G. York et al. 2000). The SV was designed to operate similarly to the Main Survey, but achieving a much higher completeness ($> 99\%$ for BGS Bright) over an area covering 180 deg^2 . In this work, we combine the BGS Bright, Faint, and SV samples to maximize the signal-to-noise ratio (SNR) of our overall SME measurement.

From the combined BGS sample, we select galaxies with reliable redshift measurements by applying a set of quality cuts. For each galaxy, we use only the best available spectrum with `ZCAT_PRIMARY==True`, and require `SPECTYPE==GALAXY`, `ZWARN==0`, and the $\Delta\chi^2$ of the best-fitting redshift above 40 (C. Hahn et al. 2023). We further impose a maximum redshift of $z=0.487$ to ensure that the [N II] $\lambda 6584$ lines of all galaxies remain fully within the DESI spectral coverage (3600Å-9800Å). After these redshift cuts, our galaxy sample is reduced by 24.9% to 5,007,186 galaxies, including 4,462,800 from BGS Bright, 254,594 from BGS Faint, and 289,792 from SV.

The galaxy properties (e.g., stellar mass and SFR) are derived from the combined DESI photometry and spectroscopy using the FASTSPECFIT²⁵ (J. Moustakas et al. 2023) pipeline. In this work, we use version v2.1 of the FASTSPECFIT catalog of DR1 galaxies, which has already been made public as part of DR1 (DESI Collaboration et al. 2025). For the stellar population synthesis modeling, FASTSPECFIT assumes a G. Chabrier (2003) initial mass function (IMF), a constant solar metallicity, and a non-parametric star formation history (SFH) with bursts.

We adopt the flux measurements of emission lines ($H\alpha$, $H\beta$, [O III] $\lambda 5007$, [N II] $\lambda 6584$). Regions with extreme reddening values ($E(B - V) > 0.8$) are excluded from this analysis. We then correct for the intrinsic dust extinction (i.e., due to the host galaxy) using the Balmer decrement, assuming case B recombination ($H\alpha/H\beta=2.87$) and the extinction law of J. A. Cardelli et al. (1989).

²⁵ <https://fastspecfit.readthedocs.io/en/latest/>

To select the star-forming galaxies, we adopt the criteria from G. Kauffmann et al. (2003) based on the emission line ratios using the Baldwin–Phillips–Terlevich (BPT; J. A. Baldwin et al. 1981) diagram. This BPT selection removes 21 per cent active galactic nucleus (AGN)-like galaxies from our sample. Following F. Mannucci et al. (2010), we further apply an SNR cut of 25 on the H α lines to select star-forming galaxies with robust overall line flux measurements (with no additional SNR cuts on other emission lines). In the end, our selections result in 2,215,719 galaxies in the star-forming galaxy sample before the metallicity measurements.

2.1.2. Measurement of Gas-phase Metallicities

We measure the gas-phase metallicity (Z_{ISM}) using the “strong line” method calibrated by F. Mannucci et al. (2010, hereafter referred to as M10). The M10 method makes use of the flux ratios of two sets of strong emission lines: N2 \equiv [N II] λ 6584/H α and R23 \equiv ([O II] λ 3727+[O III] λ 4958, 5007)/H β . In particular, the mapping between the line ratio and ISM metallicity is

$$\log R = a_0 + a_1x + a_2x^2 + a_3x^3, \quad (1)$$

where R is either N2 or R23, and $x \equiv Z_{\text{ISM}} - 8.69$ is the ISM metallicity minus the solar value $Z_{\odot} = 8.69$. The two sets of coefficients are $\{a_0, a_1, a_2, a_3\} = \{-0.683, 0.899, -0.523, -0.220\}$ and $\{0.718, -0.695, -0.622, -0.063\}$ for N2 and R23 diagnostics, respectively. Following M10, we only keep galaxies with both line ratios within their respective calibration ranges ($\log(\text{N2}) < 0.35$ and $\log(\text{R23}) < 0.90$) and the difference between two metallicity estimates within 0.25 dex. This M10-specific selection reduces the size of the star-forming galaxy sample to 1,532,313 galaxies with robust metallicity measurements. We adopt the average of the two metallicity estimates as our gas-phase metallicity Z_{ISM} for each galaxy.

We do not apply any aperture corrections to the metallicity measurements. Since the emission line fluxes are measured from within the DESI fiber radius (1.5 arcsec), which corresponds to a comoving radius $\sim 4 \text{ kpc}/h$ at $z=0.2$, we are effectively measuring the metallicities in the central regions of galaxies. Meanwhile, the stellar masses derived from FASTSPECFIT correspond to the total stellar mass of each galaxy. Consequently, any mass loss in the outer regions does not affect our measured metallicities. We have also measured the overall SME profiles using another strong line-based method calibrated by M. Curti et al. (2020) and the electron temperature-based direct method B. H. Andrews

& P. Martini (2013). The three measured SME profiles are consistent with one another, and the detailed comparison between the three sets of measurements will be presented in paper II.

2.1.3. The DESI Cluster Sample

To characterize the cluster environment, we employ the X. Yang et al. (2021, hereafter Y21) group catalog derived by applying an adaptive halo-based group finder to the DESI Legacy Imaging Surveys DR9 (A. Dey et al. 2019). The Y21 group finder is primarily based on the photometric redshifts of galaxies, but has incorporated all DESI spectroscopic redshifts up to DESI DR2. The halo masses (M_h) in the catalog are obtained via abundance matching, derived from the rank-order of the total galaxy luminosities. The corresponding halo radii ($r_{180\text{m}}$) assume a spherical overdensity-based halo definition so that the average halo density within $r_{180\text{m}}$ is 180 times the mean density of the Universe. To probe the environmental effects across a wide halo mass range, we select all the groups with $M_h > 10^{12} h^{-1} M_{\odot}$ and richness > 3 for our SME measurement. While the halo masses of most of the groups are below $10^{14} h^{-1} M_{\odot}$ (i.e., the conventional mass threshold for a cluster), we do not make any distinction between groups and clusters and use them interchangeably in this paper. We adopt the coordinates of the brightest cluster galaxies (BCGs) as the cluster centers, and define the scaled cluster-centric radius as $R_{\text{scale}} \equiv R_p / r_{180\text{m}}$, where R_p is the projected cluster-centric distance.

The metallicity enhancement of cluster galaxies (i.e., $R_{\text{scale}} < 1$) likely begins long before they first cross the cluster boundary (A. I. Zabludoff & J. S. Mulchaey 1998; Y. Fujita 2004). To capture this “chemical pre-processing” effect (A. Gupta et al. 2018) in our SME measurements, we define an “extended cluster environment” using a cylindrical volume centered on each BCG with a projected radius of $10 \times r_{180\text{m}}$ (i.e., $R_{\text{scale}} < 10$) and a line-of-sight velocity height of $\pm 1500 \text{ km/s}$. For simplicity, we apply the “satellite” label to all galaxies within this cylinder, although they mostly lie beyond the formal halo boundary. Meanwhile, we apply the “field” label to random galaxies drawn from our star-forming sample, without any selection on R_{scale} .

2.2. Measurement of the SME Profiles

We measure the overall SME profile $\Delta Z_{\text{ISM}}(R_{\text{scale}})$ from DESI as

$$\Delta Z_{\text{ISM}}(R_{\text{scale}}) = Z_{\text{ISM}}^{\text{SAT}}(R_{\text{scale}}) - Z_{\text{ISM}}^{\text{CTR}}(R_{\text{scale}}), \quad (2)$$

where $Z_{\text{ISM}}^{\text{SAT}}$ and $Z_{\text{ISM}}^{\text{CTR}}$ are the average ISM metallicities of the satellite galaxies at R_{scale} and field galaxies with

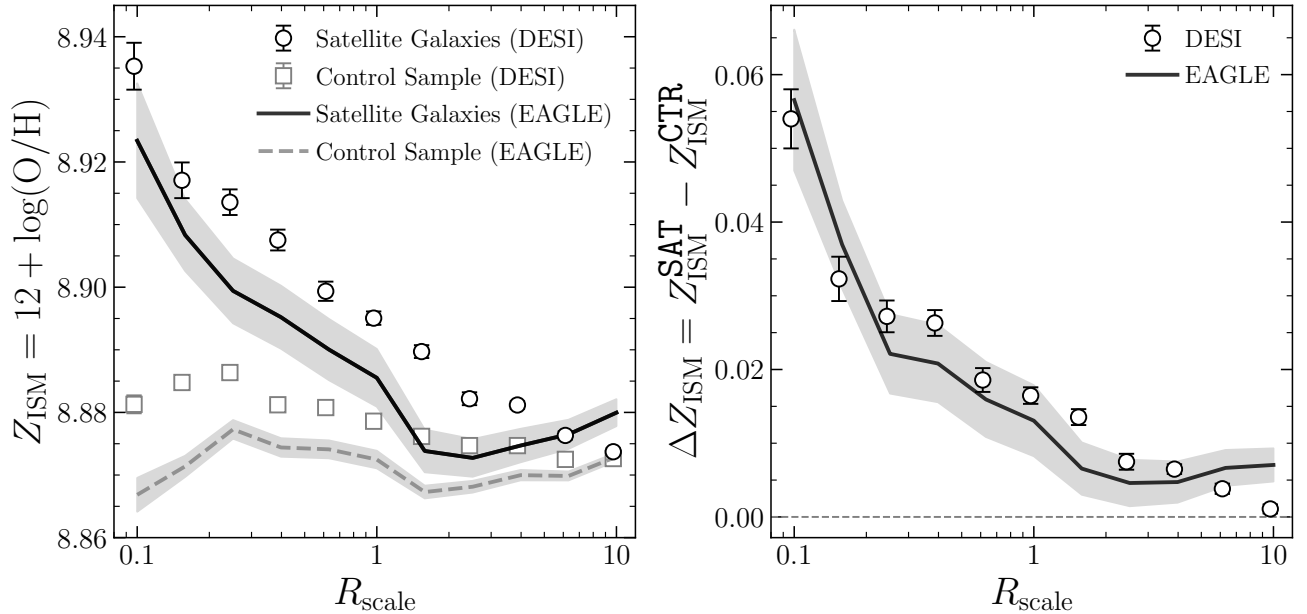


Figure 1. Comparison between the average gas-phase metallicity (left) and SME (right) profiles measured in DESI DR1 and the EAGLE simulation. Left: Average metallicity of the satellite (black open circles with errorbars) and control (gray squares with errorbars) samples as functions of projected radius R_{scale} (scaled by halo radius) measured in DESI DR1. Black solid (gray dashed) curve with an uncertainty band is the average metallicity profiles of satellite (control) galaxies in EAGLE. Right: The SME profiles derived from the left panel for DESI (black open circles with errorbars) and EAGLE (black solid curve with an uncertainty band).

similar properties in the control sample, respectively. Therefore, the key to robustly measuring SME profiles is to construct a proper control sample at any given R_{scale} . Since the metallicity of a typical field galaxy is primarily determined by its observed M_* and SFR (by virtue of the tight FMR), we construct a control sample of field galaxies for each satellite sample at R_{scale} by matching their joint 3D probability density distributions (PDFs) of $P^{\text{SAT}}(M_*, \text{SFR}, z | R_{\text{scale}}) = P^{\text{CTR}}(M_*, \text{SFR}, z | R_{\text{scale}})$. To reduce the statistical noise in the ΔZ_{ISM} measurements, we require that the size of the control sample to be at least ten times as larger as that of the satellite sample at each R_{scale} . Consequently, the ΔZ_{ISM} measured from Equation 2 can be safely interpreted as the excess metallicity of satellite galaxies acquired due to various physical processes in the extended cluster environment.

We use the EAGLE simulation to derive analytical insights into the physical processes governing the SME profiles observed by DESI. The EAGLE suite of cosmological simulations comprises a series of hydrodynamical simulations with different box sizes, particle numbers, and subgrid physics (J. Schaye et al. 2015; R. A. Crain et al. 2015). In this work, we employ the “Ref-L100N1504” simulation, which is a box of 100 Mpc (comoving) on a side with 2×1504^3 particles (equal number of dark matter and baryon particles). The particle mass is $1.81 \times 10^6 h^{-1} M_{\odot}$ for gas/stars and $9.70 \times 10^6 h^{-1} M_{\odot}$

for dark matter. This ‘reference’ model has successfully reproduced several key scaling relations of galaxies, including the galaxy stellar mass function, stellar-to-halo mass relation, and MZR (P. S. Behroozi et al. 2013; M. Furlong et al. 2015; J. Schaye et al. 2015; M. E. De Rossi et al. 2017). More important, LZ23 used the “Ref-L100N1504” simulation to demonstrate that the NEMO model accurately describes the chemical enrichment of *field* galaxies in EAGLE, providing a baseline framework for understanding the metallicity enhancement of EAGLE *satellite* galaxies.

To measure the overall SME profile in EAGLE, we select all the star-forming (SFR > 0) galaxies with $M_* > 10^8 M_{\odot}$ from the $z=0.1$ snapshot of the simulation. Following LZ23, we measure the ISM metallicities of EAGLE galaxies using $Z_{\text{ISM}} \equiv 12 + \log(Z_{\text{O}}/Z_{\text{H}}/16)$, where Z_{O} and Z_{H} are the oxygen and hydrogen mass fractions, respectively, in the ISM particles²⁶. Halos in the EAGLE simulation are identified as Friends-of-Friends (FoF) groups with $r_{200\text{m}}$ (roughly 5% smaller than $r_{180\text{m}}$) as the halo radii. We select the FOF groups with $M_h > 10^{12} M_{\odot}$ as our EAGLE cluster sample and adopt the same scheme of constructing con-

²⁶ This differs from LZ23, where a constant $Z_{\text{H}}=0.7$ was adopted to simplify the analytic model.

control samples when measuring ΔZ_{ISM} around these EAGLE clusters. To facilitate the SME comparison between DESI and EAGLE, we first measure the SME profile $\Delta Z_{\text{ISM}}(R_{\text{scale}})$ as a function of projected distance $R_{\text{scale}} \equiv R/r_{200\text{m}}$ in EAGLE, but switch to the isotropic SME profile $\Delta Z_{\text{ISM}}(r_{\text{scale}})$ as a function of the 3D scaled-distance ($r_{\text{scale}} \equiv r/r_{200\text{m}}$) when building the satellite NE-CEM model in the next Section.

2.3. SME comparison between DESI and EAGLE

We compare the measurements of SME profiles between DESI and EAGLE in Figure 1. In the left panel, black circles and gray squares with errorbars are the metallicity profiles of the DESI satellite and control samples, respectively. All errorbar are computed from Jackknife resampling in both DESI and EAGLE. The metallicity profile of the control sample does not stay flat with R_{scale} , because $P^{\text{SAT}}(M_*, \text{SFR}, z|R_{\text{scale}})$ varies from one R_{scale} bin to another. For the same reason, the declining trend of the satellite metallicity profile is partly induced by the spatial variation in the composition of the satellite population. Black solid and gray dashed curves with uncertainty bands are the corresponding measurements from EAGLE.

The corresponding SME profiles are thus measured as the metallicity difference between the satellite and control samples, shown in the right panel of Figure 1. Although both the amplitude and shape of the two EAGLE metallicity profiles are different from the DESI measurements in the left panel, the SME profile $\Delta Z_{\text{ISM}}(R_{\text{scale}})$ predicted by EAGLE (solid circles) is remarkably similar to that measured from DESI galaxies (open circles). In particular, both ΔZ_{ISM} profiles exhibit three distinct regimes of metallicity enhancement: a steep fall-off with increasing radius at $R_{\text{scale}} < 0.3$, a slow decline across halo boundary between $R_{\text{scale}} = 0.3$ and $R_{\text{scale}} = 2$, and a weak but non-zero excess beyond $R_{\text{scale}} = 2$. On the very large scales around $R_{\text{scale}} \sim 10$, the DESI profile steadily declines to zero; the EAGLE profile exhibits a plateau that stays positive, though the Jackknife errors in EAGLE are likely underestimated on those scales due to cosmic variance.

The strong agreement between the DESI and EAGLE SME profiles is highly nontrivial. This suggests the subgrid physics model in EAGLE successfully reproduces the *excess* enrichment experienced by DESI galaxies in cluster environments. To identify the dominant mechanisms responsible for this agreement, we decompose the EAGLE SME profile at $z=0.1$ into contributions from mass-loss, suppressed SF, and enriched inflow. In addition, we expect the three SME regimes exhibited in the 2D projected space (R_{scale}) to be more sharply defined

in the 3D real space (i.e., using the 3D scaled cluster-centric distance r_{scale}). Therefore, we will focus exclusively on the EAGLE simulation and switch to the 3D isotropic SME profiles $\Delta Z_{\text{ISM}}(r_{\text{scale}})$ for the rest of the paper until Figure 8, where we project the 3D decomposition into 2D to reproduce the DESI SME observation.

3. NON-EQUILIBRIUM CHEMICAL EVOLUTION MODEL FOR SATELLITE GALAXIES

3.1. Components of a Satellite NE-CEM

LZ23 demonstrated that the NE-CEM accurately describes the CEH of field galaxies in the EAGLE simulation and successfully reproduces the FMR in both EAGLE and SDSS. In this section, we adapt the NE-CEM framework to build a satellite NE-CEM by adding physics specific to the cluster environment: suppressed SF, and mass loss, and enriched inflow.

Among the three processes, suppressed SF is the most straightforward to model. We have verified that both the field and satellite galaxies in EAGLE follow the four parameter ‘‘power-law exponential’’ (hereafter shortened as **powexp**) form of SFH,

$$\dot{M}_*(t) = \dot{M}_{*,0} \left(\frac{t - t_0}{\tau_{\text{sfh}}} \right)^\kappa \exp \left(-\frac{t - t_0}{\tau_{\text{sfh}}} \right), \quad (3)$$

where t_0 represents the formation time of the galaxy. This functional form exhibits a power-law rise with slope κ followed by an exponential decline with a characteristic timescale τ_{sfh} . As LZ23 noted, Equation 3 has only two free parameters once the total formed mass and SFR at the observed epoch are specified. This constraint implies that the average SFH of satellite galaxies likely has a shallower κ and a shorter τ_{sfh} than their field counterparts, resulting in suppressed SF at the later epochs. Since an accurate description of SF suppression is required for a clean SME decomposition, we directly adopt the best-fitting **powexp** SFHs for satellite galaxies derived from EAGLE, deferring an analytic satellite SFH model to Paper III.

Regarding mass loss in satellites at a given r_{scale} , the dominant physical mechanism is tidal stripping, which generally only incurs mass loss beyond the tidal radius r_t . Consequently, tidal mass loss does not affect our metallicities observed in the central regions by DESI fibers²⁷. However, it reduces the total stellar mass of the system, thereby indirectly elevating the satellite metallicities relative to their field counterparts. For the sake of accuracy, we directly measure the average mass loss

²⁷ Mass loss in the galaxy outskirts directly affects the aperture-integrated metallicities due to non-zero metallicity gradients (D. Zaritsky et al. 1994; X. Wang et al. 2019).

for each satellite sample at r_{scale} in this work, deferring an analytic mass-loss model to Paper III.

For incorporating enriched inflows in the satellite NE-CEM, we update the original NE-CEM to allow accreted gas to have arbitrary metallicity. LZ23 assumed that accreted gas is chemically pristine. While this is likely adequate for field galaxies, it requires modification for satellite galaxies, which can actively accrete from the enriched ICM. A large inflow of pristine gas can significantly dilute the ISM metallicity, but in satellites, the accreted gas is already enriched. To model this effect, we allow the satellite NE-CEM to switch, for instance, from a pristine inflow before infall to an enriched one afterwards. Therefore, the duration of enriched inflow for a satellite is equivalent to its time spent in the cluster since infall, τ_{infall} . We expect this infall time $\tau_{\text{infall}}(r_{\text{scale}})$ to be primarily determined by dynamical friction.

Below we describe our satellite NE-CEM framework that incorporates enriched inflow.

3.2. Updated NE-CEM with enriched inflow

To model the amount of metals brought in the ISM by enriched inflow, we need an explicit prescription for the gas accretion rate \dot{M}_{inf} . However, \dot{M}_{inf} in NE-CEM is not modeled directly but implicitly through the time evolution of the gas reservoir. In particular, NE-CEM ties the mass of the star-forming gas M_{gas} at any epoch t to SFR via a volumetric Schmidt law (R. C. Kennicutt 1998)

$$M_{\text{gas}} = M_{\text{g},0} \dot{M}_{*}^{\epsilon}, \quad (4)$$

where the best-fitting parameters for EAGLE are $\log(M_{\text{g},0}/M_{\odot})=9.25\pm 0.07$ and $\epsilon=0.93\pm 0.05$. The time derivative of the gas mass is governed by star formation, galactic outflows, and gas accretion,

$$\dot{M}_{\text{gas}} = -(1 - f_{\text{rec}})\dot{M}_{*} - \dot{M}_{\text{out}} + \dot{M}_{\text{inf}}, \quad (5)$$

where f_{rec} is the IMF-averaged recycle fraction, defined as the fraction of mass formed into stars that is returned to the ISM by supernovae and evolved stars, \dot{M}_{out} and \dot{M}_{inf} represent the outflowing and inflowing rates of gas, respectively. To characterize the strength of outflows, we define the dimensionless mass-loading factor as $\eta \equiv \dot{M}_{\text{out}}/\text{SFR}$. Rearranging the preceding equation with this definition provides an expression for the gas accretion rate,

$$\dot{M}_{\text{inf}} = \dot{M}_{\text{gas}} + (1 - f_{\text{rec}})\dot{M}_{*} + \eta\dot{M}_{*}. \quad (6)$$

LZ23 used a fitting formula (their Eqn. 20) to describe the dependence of mass-loading η on M_{*} and specific SFR ($s\text{SFR}$) for the outflows in regular star-forming galaxies. However, our satellite samples include many star-forming but “almost-quenched” (i.e.,

with $s\text{SFR} < 10^{-11} \text{ yr}^{-1}$) galaxies that do not follow the LZ23 fitting formula (at least in EAGLE). To better describe outflows in those galaxies, we update the best-fitting formula of mass-loading from LZ23 as

$$\log\left(\frac{\eta}{\eta_0}\right) = f\left(\frac{M_{*}}{M_{*,0}}\right)^{\alpha}\left(\frac{s\text{SFR}}{s\text{SFR}_0}\right)^{\tilde{\beta}} \quad (7)$$

where we set $f=0.49$, $\log \eta_0=-0.2$, $\log M_{*,0}=9.5$, and $\log s\text{SFR}_0=-9.5$. For galaxies with $s\text{SFR} \geq 10^{-11} \text{ yr}^{-1}$, we adopt $\alpha=-0.15\pm 0.02$ and $\tilde{\beta}=0.29\pm 0.08$, and Equation 7 is thus equivalent with the Eqn. 20 in LZ23; for the “almost-quenched” galaxies, we find that $\tilde{\beta} = 0.5 \times \log(s\text{SFR}/10^{-11} \text{ yr}^{-1}) + 0.29$ provides a significantly better fit to the Eqn. 20 in LZ23.

Meanwhile, the time evolution of oxygen mass in the ISM (M_{O}) is

$$\dot{M}_{\text{O}} = m_{\text{O}}^{\text{cc}}\dot{M}_{*} - (1 - f_{\text{rec}})Z_{\text{O}}\dot{M}_{*} - \eta Z_{\text{O}}\dot{M}_{*} + Z_{\text{inf}}\dot{M}_{\text{inf}}, \quad (8)$$

where m_{O}^{cc} is the IMF-averaged oxygen yield, defined as the mass of oxygen produced by core-collapse supernovae (CCSNe) and returned to the ISM per solar mass of star formation, and Z_{O} and Z_{inf} are the oxygen mass fractions in the ISM and inflowing gas, respectively. On the right-hand side (RHS) of Equation 8, the four terms represent the oxygen injected by CCSNe, incorporated into stars, ejected through galactic winds, and accreted via gas inflow, respectively. Note that LZ23 adopted $Z_{\text{inf}}=0$ for field galaxies. For modeling enriched inflows, we define the “oxygen fraction ratio” (OFR) between inflowing gas and ISM as

$$f_{\text{inflow}}(t) = \frac{Z_{\text{inf}}(t)}{Z_{\text{O}}(t)}, \quad (9)$$

and expect $0 < f_{\text{inflow}} < 1$ in the cluster environment.

In order to track the CEH of satellite galaxies, the key equation is the time derivative of Z_{O} ,

$$\frac{dZ_{\text{O}}}{dt} = \frac{\dot{M}_{\text{O}}}{M_{\text{gas}}} - \frac{\dot{M}_{\text{gas}}}{M_{\text{gas}}}Z_{\text{O}}. \quad (10)$$

Plugging Equation 6, 8 and 9 into Equation 10, we arrive at

$$\frac{dZ_{\text{O}}}{dt} = \frac{m_{\text{O}}^{\text{cc}}}{\tau_{*}} - (1 - f_{\text{inflow}})Z_{\text{O}}\left(\frac{1}{\tau_{\text{dep}}} + \frac{\ddot{M}_{*}}{\dot{M}_{*}} + \frac{\dot{\tau}_{*}}{\tau_{*}}\right). \quad (11)$$

where $\tau_{*} \equiv M_{\text{gas}}/\dot{M}_{*}$ is the gas consumption timescale and $\tau_{\text{dep}} \equiv \tau_{*}/(1 + \eta - r)$ is the gas depletion timescale. For constant τ_{*} and η , the ISM oxygen abundance would asymptotically approach an equilibrium value:

$$Z_{\text{O,eq}} = \frac{m_{\text{O}}^{\text{cc}}}{(1 - f_{\text{inflow}})\tau_{*}} \tilde{\tau}, \quad (12)$$

where $\tilde{\tau}$ is the ‘‘harmonic difference timescale’’

$$\tilde{\tau} \equiv \frac{1}{\tau_{\text{dep}}^{-1} - \tau_{\text{sfh}}^{-1}}, \quad (13)$$

introduced by D. H. Weinberg et al. (2017). Therefore, an enriched inflow boosts the equilibrium oxygen fraction of the ISM by $1/(1-f_{\text{inflow}})$ compared to a pristine one.

This updated NE-CEM with arbitrary f_{inflow} provides us a generic framework for tracking the metallicity evolution of both satellite and field galaxies. In particular, for a given satellite sample at r_{scale} , we solve for its average CEH using Equation 11 assuming a time-varying f_{inflow} . For the metallicity evolution of field galaxies, we adopt the original NE-CEM from LZ23, which is equivalent to solving for Equation 11 assuming a constant f_{inflow} without mass loss.

4. MATHEMATICAL DECOMPOSITION OF THE SME

To ensure a *clean* SME decomposition, we first design a parallel set of controlled experiments to unambiguously reveal the SME contribution from one *single* physical process at a time (i.e., a mathematical decomposition). Next, we use our satellite NE-CEM to clarify the underlying physics behind the mathematical decomposition, presenting a robust physical decomposition of the SME profile.

4.1. Field Galaxies with Properties Matched to Satellite Galaxies

In this subsection, we set the stage for the controlled experiments by defining three reference samples from the field galaxies in the simulation.

We start by measuring a set of physical quantities associated with star-forming satellite galaxies in the simulation. In particular, for a satellite galaxy observed at $z=0.1$, we follow the practice in LZ23 and measure the in-situ SFH ($\dot{M}_*(t)$) by summing the SFRs of all its progenitors at the same epoch t , instead of considering only the main branch. The SFR observed at $z=0.1$ is thus

$$\text{SFR}^{\text{obs}} \equiv \dot{M}_*(t = t_{0.1}), \quad (14)$$

where $t_{0.1}=12.45$ Gyr is the age of the Universe at $z=0.1$. From this SFH, we compute a *formed* stellar mass as a function of time t as

$$M_*^{\text{fmd}}(t) = \int_0^t (1 - f_{\text{rec}}) \dot{M}_*(t') dt'. \quad (15)$$

In an isolated field environment, the total mass of stars of a galaxy has ever formed by t , $M_*^{\text{fmd}}(t)$, is equal to the *retained* mass at that epoch, $M_*^{\text{ret}}(t)$, hence

$$M_*^{\text{ret}}(t) = M_*^{\text{fmd}}(t) \quad \text{for field galaxies.} \quad (16)$$

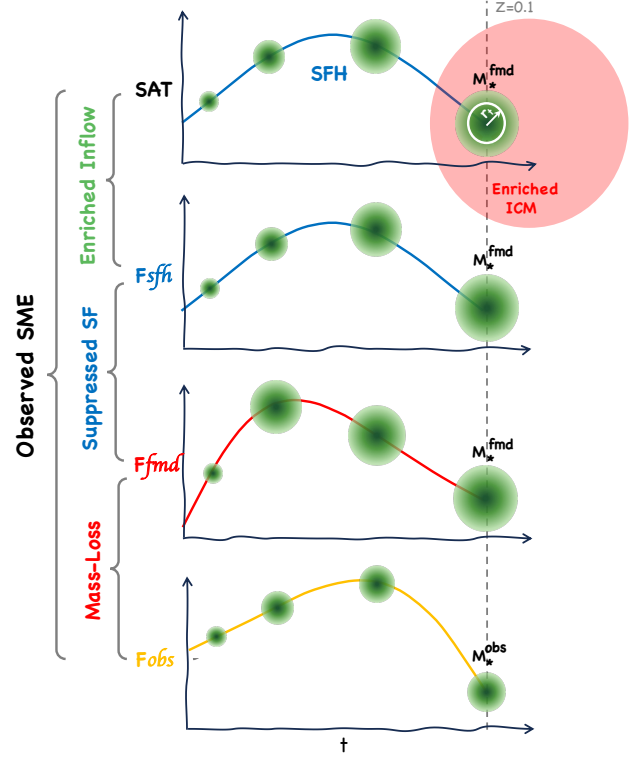


Figure 2. A cartoon version of Equation 20, decomposing the observed SME into contributions due to three different physical processes (annotated on the left). Each panel illustrates the typical evolutionary trajectory of a galaxy from one of the four samples in Table 1 (from top to bottom: SAT, Fsfh, Ffmd, Fobs). The SFH is traced by the colored curve, through which the four green disks denote the stellar mass growth, with the disk size proportional to the formed mass $M_*^{\text{fmd}}(t)$. In the top panel, a SAT galaxy enters into the cluster at the final epoch ($z=0.1$), with its disk truncated at the tidal radius r_t (solid white circle) and embedded in the enriched ICM (red sphere). The stellar mass loss is thus indicated by the difference between M_*^{fmd} and M_*^{obs} (mass enclosed within r_t). The Fsfh, Ffmd, and Fobs are field galaxies matched to the SAT by SFH, M_*^{fmd} , and M_*^{obs} , respectively.

However, a satellite galaxy usually has $M_*^{\text{ret}}(t) < M_*^{\text{fmd}}(t)$, and the difference between the two

$$\Delta M_*(t) = M_*^{\text{fmd}}(t) - M_*^{\text{ret}}(t), \quad (17)$$

quantifies the accumulated stellar mass-loss as a function of t , primarily due to tidal stripping in the cluster environment. For quantifying the physical state of each satellite galaxy with SFR^{obs} at $z=0.1$, we define the following three *state variables*:

$$\begin{aligned} M_*^{\text{obs}} &\equiv M_*^{\text{ret}}(t = t_{0.1}), \\ M_*^{\text{fmd}} &\equiv M_*^{\text{fmd}}(t = t_{0.1}), \\ \text{SFH} &\equiv \dot{M}_*(t < t_{0.1}), \end{aligned} \quad (18)$$

Table 1. Properties of four galaxy samples used for SME decomposition. Note that all four samples are additionally match in SFR^{obs} .

Sample	Environment	Properties
SAT	Cluster	$P(M_*^{\text{obs}}, M_*^{\text{fmd}}, \text{SFH})$
Fsfh	Field	$P(\text{SFH})$ matched to SAT
Ffmd	Field	$P(M_*^{\text{fmd}})$ matched to SAT
Fobs	Field	$P(M_*^{\text{obs}})$ matched to SAT

where SFH is a vector variable measured from all the simulation snapshots before $z=0.1$. At any given r_{scale} , we thus characterize the satellite galaxy sample using $P(M_*^{\text{ret}}, M_*^{\text{fmd}}, \text{SFH})$, the joint distribution of M_*^{ret} , M_*^{fmd} and SFH of that sample. Accordingly, we define three types of reference samples using the field galaxies (*Fobs*, *Ffmd*, and *Fsfh*), each with the PDF of one state variable matched to that of the satellite sample (SAT). In addition, we ensure that all the four samples have the same $P(\text{SFR}^{\text{obs}})$. The properties of the four samples are summarized in Table 1.

Note that the *Fobs* sample is equivalent to the CTR sample we constructed in §2.2 when measuring the projected SME profiles in DESI. However, it is impossible to construct the *Ffmd* and *Fsfh* samples in the observations, while using the EAGLE simulation allows us to construct all three reference samples from the simulated mock galaxies. As will be shown, our SME decomposition at each r_{scale} depends critically on comparisons among different samples in Table 1.

4.2. From Mathematical Decomposition to Physical Processes

We measure the 3D isotropic SME profile from the EAGLE simulation as

$$\Delta Z_{\text{ISM}}(r_{\text{scale}}) = Z_{\text{ISM}}^{\text{SAT}}(r_{\text{scale}}) - Z_{\text{ISM}}^{\text{Fobs}}(r_{\text{scale}}). \quad (19)$$

At each r_{scale} , the RHS of the above equation can be mathematically separated into three terms as

$$\Delta Z_{\text{ISM}} = \underbrace{(Z^{\text{SAT}} - Z^{\text{Fsfh}})}_{\text{Enriched Inflow}} + \underbrace{(Z^{\text{Fsfh}} - Z^{\text{Ffmd}})}_{\text{Suppressed SF}} + \underbrace{(Z^{\text{Ffmd}} - Z^{\text{Fobs}})}_{\text{Mass-Loss}}, \quad (20)$$

where the text below each term describes the physical process responsible for that term (as will be explained further below). We omit the subscripts on the RHS of Equation 20 to avoid clutter.

Equation 20 provides the mathematical basis for our physically-motivated SME model. To illustrate this, Figure 2 uses schematic diagrams to demonstrate how

each term in Equation 20 emerges from the three underlying physical processes. The four panels depict the evolutionary path of a typical galaxy from each of the four galaxy samples (from top to bottom: SAT, *Fsfh*, *Ffmd*, *Fobs*). In each panel, the solid curve tracks the SFH of the galaxy on the SFR vs. t diagram, arriving at the same SFR^{obs} at $z=0.1$; the four green circular disks along the SFH curve represent the growth history of the galaxy through four epochs, with the disk sizes proportional to $M_*^{\text{fmd}}(t)$.

In the top panel of Figure 2, a SAT galaxy has recently fallen into a cluster (red sphere) and is thus embedded in the metal-enriched ICM at $z=0.1$. During the process, the SAT galaxy loses all the stellar mass beyond its tidal radius (r_t), denoted by the white circle within the green disk. Consequently, the mass enclosed within the white circle is the observed (i.e., retained) mass M_*^{ret} , whereas the total mass of the green disk is the formed mass M_*^{fmd} .

In the three bottom panels, each cartoon galaxy represents a field galaxy that has one state variable in Equation 18 exactly matched to the SAT galaxy, highlighting one particular physical process (annotated vertically on the left) that contributes to the observed SME. We describe them as follows.

- Enriched inflow (second panel): an *Fsfh* galaxy follows exactly the same SFH (blue curve) as that of the SAT galaxy, but remained isolated in the field. Therefore, the main²⁸ difference in the metal enrichment between SAT and *Fsfh* is whether the galaxy has accreted metal-enriched gas from the ICM in the last τ_{infall} Gyr, contributing to the SME profile as the “enriched inflow” component (i.e., $Z^{\text{SAT}} - Z^{\text{Fsfh}}$).
- Suppressed SF (third panel): an *Ffmd* galaxy has arrived at the same M_*^{fmd} as that of *Fsfh*, but follows the typical SFH (red curve) of galaxies in the field rather than that of the SAT galaxy. The metallicity difference between *Ffmd* and *Fsfh* is thus the SME contribution due to “suppressed SF” (i.e., $Z^{\text{Fsfh}} - Z^{\text{Ffmd}}$).
- Mass-loss (fourth panel): an *Fobs* galaxy is a typical galaxy in the field with its stellar mass equal to M_*^{obs} (i.e., the enclosed mass of the SAT galaxy within r_t). Since the *Fobs* galaxy has a lower mass, it likely has a younger stellar age (orange curve) than the *Ffmd* due to the so-called “downsizing”

²⁸ The mass-loading histories are slightly different due to the stellar mass loss of the SAT galaxy.

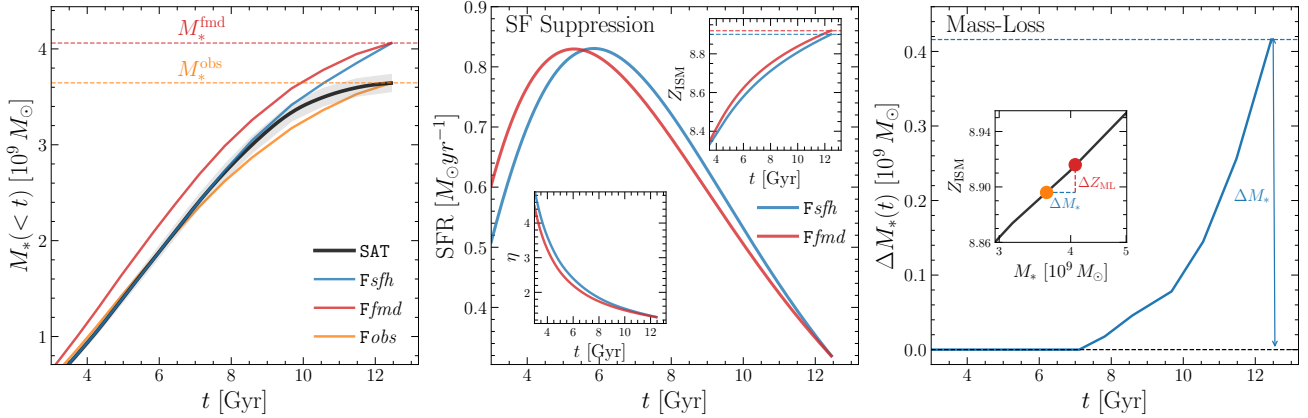


Figure 3. The average stellar mass growth (left), star formation (middle), and mass loss (right) histories of relevant EAGLE galaxy samples at $r_{\text{scale}}=[0.2, 0.4]$. Left: Colored curves indicate the stellar mass evolution of SAT (black), *Fsfh* (blue), *Ffmd* (red), and *Fobs* (orange) samples. Red and orange horizontal dashed lines denote the formed and observed stellar masses of the SAT sample at $z=0.1$, respectively. Middle: Red and blue curves are the average SFHs of *Ffmd* and *Fsfh* samples, with the evolutions of their corresponding mass-loading factors and metallicities shown in the bottom-left and top-right inset panels, respectively. Right: Mass loss history of the SAT sample, computed from the difference between the blue and black curves in the left panel. The inset panel shows the MZR of galaxies with the same SFR^{obs} . Red and orange filled circles mark the location of the *Ffmd* and *Fobs* galaxies, respectively.

effect (L. L. Cowie et al. 1996). Both the *Ffmd* and *Fobs* galaxies are the typical field galaxies that land *perfectly* on the MZR, and the metallicity difference between the two can be entirely explained by their difference in M_* — hence the SME contribution from “mass-loss” (i.e., $Z^{\text{Ffmd}} - Z^{\text{Fobs}}$).

5. PHYSICAL DECOMPOSITION OF THE SME PROFILE

Having defined the three reference samples in §4.1, we now perform our physical decomposition of the SME profile using Equation 20. As indicated in Table 1, these samples are primarily distinguished by their stellar mass growth histories. Accordingly, the left panel of Figure 3 of SAT galaxies at $r_{\text{scale}}=[0.2, 0.4]$ (thick black curve) with that of the three reference samples: *Fsfh* (blue), *Ffmd* (red), and *Fobs* (orange), echoing the schematic shown in Figure 2. Note that all the curves are predicted by the best-fitting **powexp** models, which provide accurate descriptions of the measurements from EAGLE (not shown). The red and orange dashed horizontal lines mark M_*^{fmd} and M_*^{obs} , respectively.

The red curve (*Ffmd*), which represents the typical field galaxy observed with M_*^{fmd} , reaches the same *formed* mass as the blue curve (*Fsfh*) but through different SFHs. Comparing these two would reveal the impact by suppressed SF. Meanwhile, the orange curve (*Fobs*), representing the typical field galaxy observed with M_*^{obs} , should arrive at a lower metallicity than that of *Ffmd* according to the MZR. Thus, comparing these two directly along the MZR would reveal the mass loss term.

By construction, the blue curve also represents the evolution of the formed stellar mass of the SAT sample. The *retained* (black) and *formed* (blue) stellar mass evolutions of the SAT sample start diverging at $t \simeq 9$ Gyr, likely the average epoch of infall for SAT galaxies at $r_{\text{scale}}=[0.2, 0.4]$. The SAT galaxies would subsequently accrete gas from an enriched ICM. We examine the three comparisons in turn below, using the satellite sample at $r_{\text{scale}}=[0.2, 0.4]$ as an example.

5.1. Suppressed Star Formation and Mass Loss

We start our SME decomposition by examining the contribution caused by the SF suppression at $r_{\text{scale}}=[0.2, 0.4]$. The middle panel of Figure 3 shows the **powexp** SFHs of the M_*^{fmd} (red curve; *Ffmd*) and SFH-matched (blue curve; *Fsfh*) galaxies. The two best-fitting SFH parameters are $\{\dot{M}_{*,0}, t_0, \kappa, \tau_{\text{sfh}}\} = \{2.09, 0.31, 2.35, 3.07\}$ and $\{1.87, 0.98, 1.41, 2.36\}$ for *Ffmd* and *Fsfh*, respectively.

Although the two SFHs produce exactly the same final stellar mass M_*^{fmd} at $z=0.1$, the SFH of *Fsfh* galaxies (blue) follows that of the SAT galaxies, which exhibit a recent suppression after $t=9$ Gyr, consistent with the reduced molecular hydrogen content found in satellite galaxies in the EAGLE simulation (A. Manuwal & A. R. H. Stevens 2023). We predict the CEHs that correspond to the average SFHs of *Fsfh* and *Ffmd* samples, as shown by the blue and red curves, respectively, in the top-right inset panel.

Interestingly, the SME contribution due to SF suppression is negative, i.e., $Z_{\text{ISM}}^{\text{Fsfh}} - Z_{\text{ISM}}^{\text{Ffmd}} < 0$ (comparing

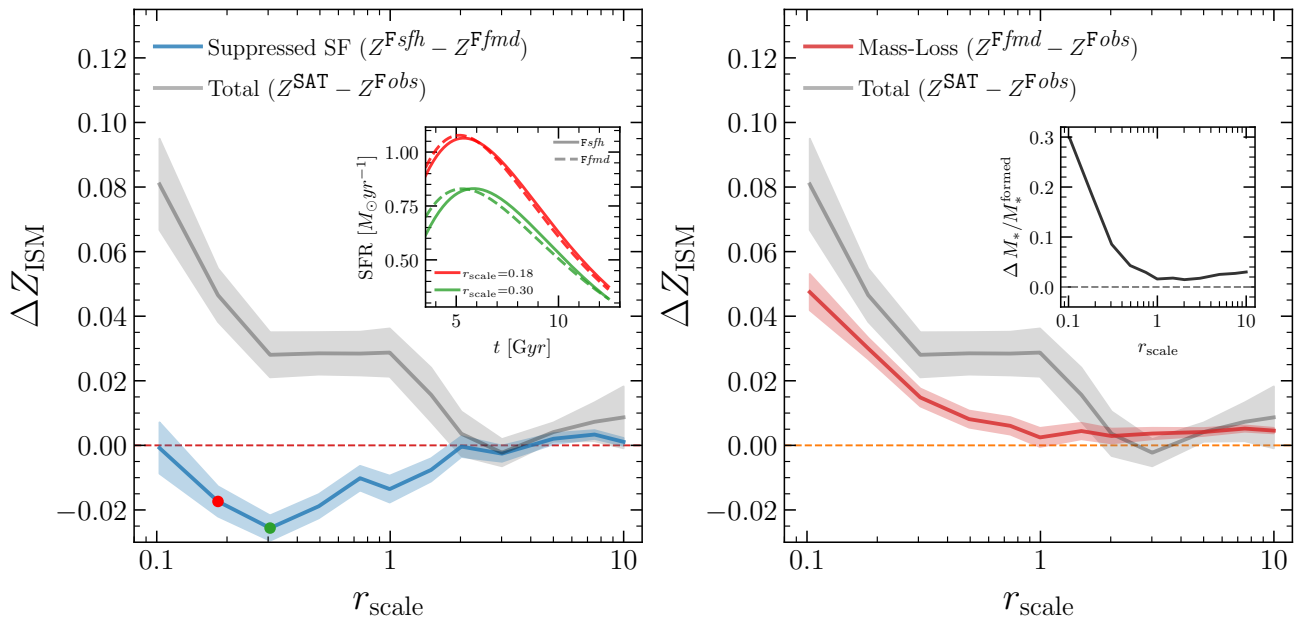


Figure 4. Contributions to the overall SME profile (gray curve in each panel) due to suppressed SF (blue curve; left panel) and stellar mass loss (red curve; right panel), as functions of the 3D scaled radius r_{scale} in EAGLE. The inset of the left panel shows the average SFHs of Fsfh (solid curves) and Ffmd (dashed curves) samples at $r_{\text{scale}}=0.18$ (red) and 0.3 (green), respectively. The inset of the right panel shows the fractional mass-loss as a function of r_{scale} for the SAT galaxy sample.

the two horizontal dashed lines in the top-right inset). This intriguing result can be readily understood using the NE-CEM framework. The Ffmd galaxies started forming stars much earlier, yielding a significantly more enriched ISM than the Fsfh sample before $t=6$ Gyr. The Fsfh galaxies began to catch up in SF at $t>6$ Gyr, but their average stellar mass remains lower than Ffmd , producing a higher mass-loading in the outflows (blue curve in the bottom left inset panel). Therefore, the chemical enrichment of the Fsfh sample remained fallen behind and fail to catch up with Ffmd by $z=0.1$.

The SME contribution due to mass-loss is illustrated in the right-most panel of Figure 3. The blue curve is the average mass-loss experienced by the SAT galaxies as a function of time, computed from the difference between the black and blue curves in the left-most panel (Equation 17). The SAT galaxies start losing a significant amount of stellar mass upon infall ($t\sim 9$ Gyr), and the fractional mass-loss reaches $\sim 10\%$ by $z=0.1$.

To convert this mass loss into a metallicity enhancement, we show the MZR (black curve; $Z_{\text{ISM}}=0.40 \times \log M_{*} + 5.07$) of EAGLE galaxies at fixed $\text{SFR}^{\text{obs}}=10^{-0.5} M_{\odot} \text{yr}^{-1}$ in the inset panel. The red and orange circles indicate the locations of two typical galaxies from the Ffmd and Fobs samples, respectively. Consequently, we directly read off the SME contribution due to mass-loss ΔM_{*} as $Z_{\text{ISM}}^{\text{Ffmd}} - Z_{\text{ISM}}^{\text{Fobs}} = 0.40 \times \Delta(\log M_{*}) = 0.015$.

Following the decomposition method outlined in Figure 3, we derive the SME contributions from the suppressed SF and mass-loss as functions of r_{scale} , shown in the left and right panels of Figure 4, respectively. In both panels, the gray curve with a shaded uncertainty band indicate the total SME profile of EAGLE satellite galaxies as a function of the 3D scaled distance r_{scale} . As expected from §2, the three distinct regimes of SME we identified from the projected profile become even more prominent in the 3D profile, exhibiting a steep inner slope at $r_{\text{scale}}<0.3$, a plateau at $0.3<r_{\text{scale}}<1$, and a shallow decline at $1<r_{\text{scale}}<3$ before eventually approaching zero at $r_{\text{scale}}>3$.

In the left panel of Figure 4, the blue curve with an error band indicates the SME contribution due to suppressed SF, derived from the metallicity difference between Fsfh and Ffmd as a function of r_{scale} .

This SME component is negative on all scales below $r_{\text{scale}}=2$ and exhibits a non-monotonic behavior, with a minimum of $\Delta Z_{\text{ISM}}=-0.022$ at $r_{\text{scale}}=0.3$. This is consistent with the “delayed-then-rapid” quenching scenario, in which galaxies experience the maximum suppression of SF right before they become rapidly quenched around $r_{\text{scale}}\sim 0.3$. Starting at the infall ($r_{\text{scale}}\sim 1$), SFH-matched galaxies (Fsfh) show little difference in SFH compared with their M_{*}^{fmd} -matched counterparts (Ffmd). As r_{scale} decreases, the SFH of satellites becomes increasingly suppressed, resulting in a growing metallicity deficit. However, once the SAT

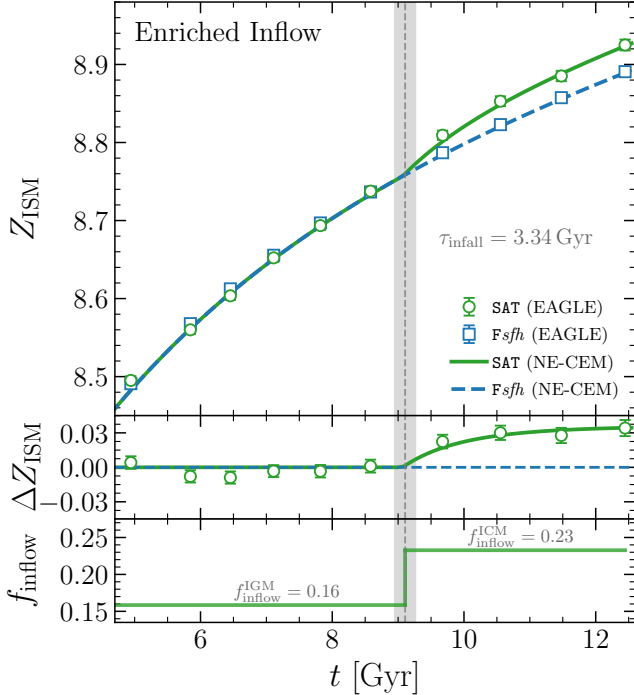


Figure 5. Satellite metallicity enhancement due to enriched inflow at $r_{\text{scale}}=[0.2, 0.4]$. Top: The average chemical enrichment histories of SAT (green circles) and Fsfh (blue squares) galaxies measured from EAGLE. Green solid curve shows the prediction from our best-fitting satellite NE-CEM with $\tau_{\text{infall}}=3.34$ Gyr and $f_{\text{inflow}}^{\text{ICM}}=0.23$, and blue dashed curve is the best-fitting prediction from a field NE-CEM with $f_{\text{inflow}}^{\text{IGM}}=0.16$. Middle: Metallicity difference between the SAT and Fsfh samples as a function of time. Bottom: The time evolution of f_{inflow} predicted by the best-fitting satellite NE-CEM model (green curve).

galaxies reach the cluster core at $r_{\text{scale}}\sim 0.3$, most have concluded the “delayed” phase of residual SF and begin to be rapidly quenched. The small number of star-forming galaxies found at $r_{\text{scale}}<0.3$ are likely systems with substantial central gas reservoirs, allowing their SFHs to remain comparable to those in the field.

To better understand the origin of this minimum, we compare the levels of SF suppression between $r_{\text{scale}}=0.3$ (green curves) and $r_{\text{scale}}=0.18$ (red curves) in the inset panel. For each r_{scale} , the SFH of the Fsfh (i.e., SFH-matched) and Ffmd ($M_{\text{star}}^{\text{fmd}}$ -matched) samples are shown by the solid and dashed curves, respectively. The average formed stellar mass of the SAT galaxies at $r_{\text{scale}}=0.18$ ($\log M_{\text{star}}^{\text{fmd}}=9.69$) is higher than that at $r_{\text{scale}}=0.3$ ($\log M_{\text{star}}^{\text{fmd}}=9.58$), consistent with the shorter timescale of dynamical friction for the more massive galaxies. This explains the higher amplitude of the SFHs at $r_{\text{scale}}=0.18$ than at $r_{\text{scale}}=0.3$. More important, the level of SF suppression at $r_{\text{scale}}=0.3$ (compare

the two green curves) is much stronger than that at $r_{\text{scale}}=0.18$ (compare the two red curves).

Switching to the right panel of Figure 4, the red curve with an uncertainty band shows the SME contribution due to mass loss, computed from the metallicity difference between the Ffmd ($M_{\text{star}}^{\text{fmd}}$ -matched) and Fobs ($M_{\text{star}}^{\text{obs}}$ -matched) samples. Unlike the suppressed SF, the mass-loss component is positive across all scales. Since the amplitude of this component is linearly proportional to the amount of mass loss at r_{scale} , the declining trend with increasing r_{scale} directly reflects the dependence of fractional mass-loss on radius, shown by the black curve in the inset panel. The infalling galaxies often started losing mass due to an enhanced tidal field and frequent fly-bys on scales about several times the halo radius (B. Moore et al. 1996), producing the positive plateau in the mass-loss component at $r_{\text{scale}}=1-10$.

Combining the two panels of Figure 4, we find that the SF-suppression and mass-loss components have similar declining shapes with increasing radius at $r_{\text{scale}}<0.3$, consistent with the sharp drop-off exhibited by the total profile in the inner region. Beyond $r_{\text{scale}}=0.3$, the two components have opposite signs but comparable amplitudes, suggesting that the sum of the two cannot explain the plateau exhibited by the total SME profile at $0.3<r_{\text{scale}}<1$. We thus expect the third contribution, i.e., enriched inflow, to be the most dominant process that boosts the metallicity of satellites on those scales.

5.2. Enriched Inflow

In order to extract the SME component due to enriched inflow, we adopt the satellite NE-CEM developed in §3 with $f_{\text{inflow}}(t)$ varying as a step-function

$$f_{\text{inflow}}(t) = \begin{cases} 0.16 & t \leq t_{0.1} - \tau_{\text{infall}} \\ f_{\text{inflow}}^{\text{ICM}} & t > t_{0.1} - \tau_{\text{infall}}, \end{cases} \quad (21)$$

where

$$\log f_{\text{inflow}}^{\text{ICM}} \equiv Z_{\text{ICM}} - Z_{\text{ISM}}, \quad (22)$$

is the metallicity difference between ICM and ISM, i.e., the logarithmic ICM-to-ISM OFR. We set the pre-infall value of f_{inflow} to be 0.16, estimated using all the star-forming field galaxies at $z=0.1$ in EAGLE. Consequently, our satellite NE-CEM has only two parameters, the infall time τ_{infall} and the ICM-to-ISM OFR $f_{\text{inflow}}^{\text{ICM}}$, while the SFH and mass loss history are directly measured from the simulation.

Figure 5 compares the CEHs of the SAT (green circles) and Fsfh (blue squares) samples at $r_{\text{scale}}=[0.2, 0.4]$, measured directly from the simulation. The blue dashed curve represents the prediction for Fsfh (i.e.,

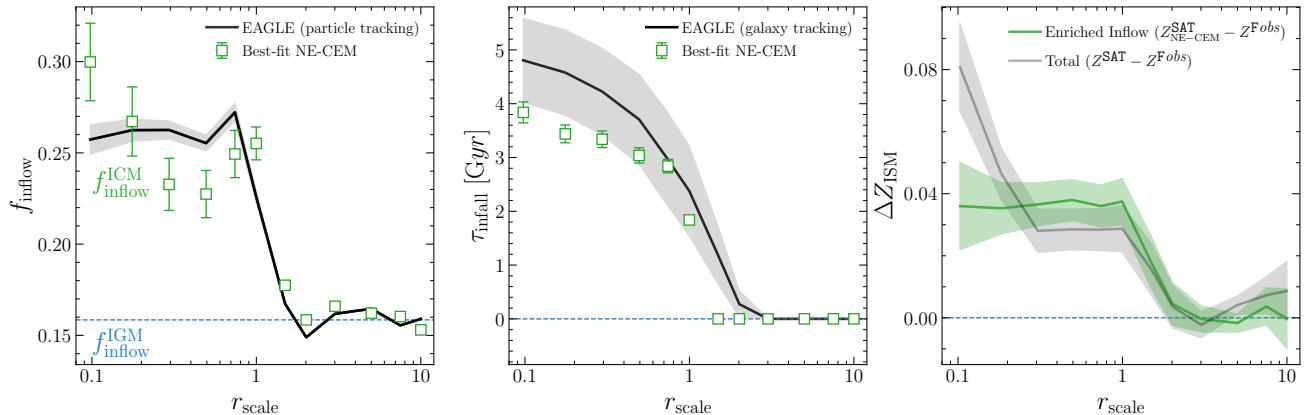


Figure 6. Contribution to the overall SME profile due to enriched inflow, as predicted by our satellite NE-CEM. Left: Oxygen fraction of the inflow (relative to the ISM) f_{inflow} as a function of r_{scale} . Black curve with a gray uncertainty band indicate the direct measurement from EAGLE, while squares with errorbars are the constraints from our satellite NE-CEM. Middle: Similar to the left panel, but for the infall time τ_{infall} . Right: Green curve with an uncertainty band indicates the SME contribution due to enriched inflow, predicted by our best-fitting satellite NE-CEM. Gray curve is the overall SME profile measured from EAGLE.

SFH-matched) from our field NE-CEM (i.e., setting $f_{\text{inflow}}^{\text{IGM}}=0.16$ in Equation 11), providing an excellent description of its CEH. Next, we fit the SAT CEH (green circles) with our satellite NE-CEM using Equation 11 and 21, while adopting the same `powexp` SFH as that used for predicting the `Fsfh` CEH. The chemically-inferred constraints on the infall timescale and ICM-to-ISM OFR are $\tau_{\text{infall}}=3.34\pm 0.15$ Gyr and $f_{\text{inflow}}^{\text{ICM}}=0.23\pm 0.02$, respectively, with the best-fitting prediction shown as the green solid curve. The middle subpanel shows the metallicity difference between the SAT and `Fsfh` samples as a function of time. Upon entering the cluster environment, satellite galaxies undergo rapid metallicity enhancement within the first gigayear, due to the sudden jump in f_{inflow} (Equation 21; green curve in the bottom subpanel). After this initial increase, the metallicity difference relative to the field remains constant until $z=0.1$. Similar to the $r_{\text{scale}}=[0.2, 0.4]$ bins shown in Figure 5, our best-fitting satellite NE-CEM provides excellent descriptions of the CEHs of SAT galaxies in all other r_{scale} bins (not shown), providing constraints on τ_{infall} and $f_{\text{inflow}}^{\text{ICM}}$ as functions of r_{scale} .

We now ask whether our chemically-inferred values of τ_{infall} and $f_{\text{inflow}}^{\text{ICM}}$ are consistent with the direct measurements from the simulation. In the left panel of Figure 6, we show our chemically-inferred $f_{\text{inflow}}^{\text{ICM}}$ in different r_{scale} bins as green squares with errorbars, while the directly-measured metallicity ratios between ICM and ISM gas particles are indicated by the black curve with a gray uncertainty band. The simulation measurement has a flat profile within $r_{\text{scale}}=0.5$, while the chemically-inferred profile shows a declining trend with increasing r_{scale} .

The cause of this discrepancy is likely complex — the chemically-inferred f_{inflow} is a somewhat CEH-averaged value over the course of the satellite evolution before reaching r_{scale} , while the simulation-measured value is instantaneous at that r_{scale} . Nevertheless, the two sets of $f_{\text{inflow}}(r_{\text{scale}})$ profiles agree reasonably well over the entire range of $0 < r_{\text{scale}} < 10$, including both the overall amplitude of f_{inflow} within $r_{\text{scale}}=1$ and the sharp transition across the halo boundary.

In the middle panel of Figure 6, we compare our chemically-inferred τ_{infall} profile (green squares with errorbars) with the direct measurement from simulation (black solid curve with an uncertainty band). We measure the average τ_{infall} of the SAT sample at different r_{scale} by tracking the main branch of a galaxy’s merger tree and identifying the epoch at which that galaxy changed its identity from being a central galaxy (`SubGroupNumber=0`) to a satellite (`SubGroupNumber>0`). The measurement uncertainty includes both the error on the mean in the sample and the error associated with the interpolation between two snapshots. The simulation-measured $\tau_{\text{infall}}(r_{\text{scale}})$ profile remains positive at $1 < r_{\text{scale}} < 2$, because the FoF clusters may have satellite beyond $r_{200\text{m}}$. Overall, the chemically-inferred τ_{infall} is shorter than the simulation measurement, but the two are roughly consistent within 1σ .

The overall agreement between the two types of measurements is encouraging, suggesting that we can potentially infer the dynamical history of satellite galaxies from their observed metallicity enhancement.

Repeating the analysis shown in Figure 5, we compute the SME contribution ($Z_{\text{ISM}}^{\text{SAT}} - Z_{\text{ISM}}^{\text{Fsfh}}$) due to en-

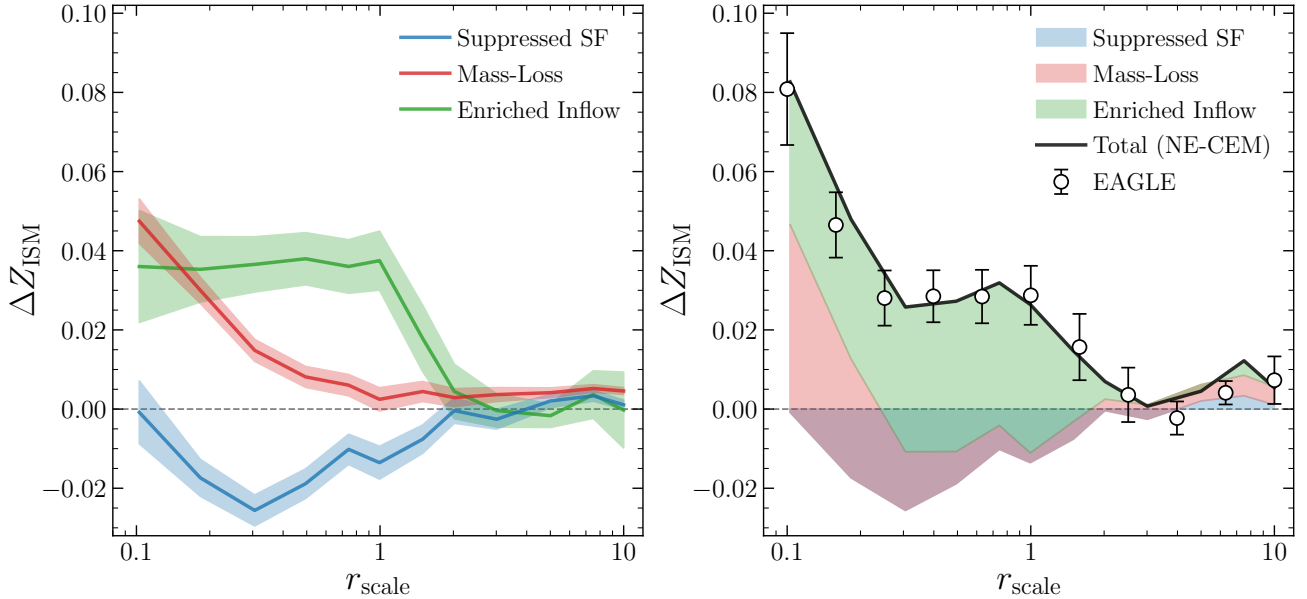


Figure 7. Final decomposition of the 3D overall SME profile in EAGLE. Left: Blue, red, and green bands indicate the SME components due to suppressed SF, mass-loss, and enriched inflow, respectively, as functions of r_{scale} . Right: Comparison between the overall SME profiles reconstructed (black curve) by stacking the three contributions (colored layers) and directly measured from EAGLE (open circles with errorbars).

riched inflow at different r_{scale} , shown as the green curve with an uncertainty band in the right panel of Figure 6. Same as in Figure 4, the gray curve with an uncertainty band represents the total SME profile in the EAGLE simulation. As we expected in §5.1, the SME component due to enriched inflow dominates the scale between $r_{\text{scale}}=0.3$ and $r_{\text{scale}}=1$, and stays flat with an amplitude of $\Delta Z_{\text{ISM}} \sim 0.037$. Beyond $r_{\text{scale}}=1$, the enriched-inflow component declines rapidly to zero at $r_{\text{scale}} \sim 2-3$.

The SME of $\Delta Z_{\text{ISM}} \sim 0.037$ can be understood as follows. From Equation 12, we expect the boost in metallicity to be $(1-0.16)/(1-f_{\text{inflow}}^{\text{ICM}}) = 1.09$ if the satellites have reached chemical equilibrium. This 9 per cent boost is consistent with $10^{\Delta Z_{\text{ISM}}} \sim 1.09$. The fact that the green curve is roughly flat within $r_{\text{scale}}=1$ indicates that the timescale for this metallicity boost due to ICM is short compared to τ_{infall} , as can be seen from the middle panel of Figure 5. Therefore, this elevation in metallicity does not require equilibrium, as most of the satellites at $r_{\text{scale}} \sim 1$ fell into clusters recently and have yet to adjust to chemical equilibrium.

5.3. Comparison of the Three SME Components

Putting all the pieces together, we summarize the results of our comprehensive SME decomposition in Figure 7. In the left panel, blue, red, and green curves with error bands indicate the SME contributions from suppressed SF, mass-loss, and enriched inflow, respectively. The three curves are derived separately earlier

in the paper according to Equation 20. We find that the three components have very different radial dependence within $r_{\text{scale}}=2$, thereby shaping the three distinct regimes in the total SME profile.

The right panel of Figure 7 provides a more visually appealing way for understanding the shape of the total SME profile. The simulation measurement is shown by the open circles with errorbars. Underneath these data points, we present a stacked version of the SME decomposition, illustrating each component by the area covered by its respective color listed in the legend. The thick black curve indicates the sum of the three contributions, which provides an excellent description of the data points measured directly from the simulation.

The enriched-inflow component dominates the SME in the outer region of the cluster between $r_{\text{scale}}=0.3-1$; but in the inner core of clusters ($r_{\text{scale}} < 0.3$), the mass-loss term starts to take over and rise towards $r_{\text{scale}}=0$. However, this SME increase due to mass-loss is largely offset by the negative contribution due to suppressed SF on scales $r_{\text{scale}}=0.3-1$. Interestingly, the suppressed-SF component has a V-shaped profile with a minimum at $r_{\text{scale}}=0.3$, possibly driven by the “delayed-then-rapid” quenching of satellites. Thus, the sharp increase of both the mass-loss and suppressed-SF components towards $r_{\text{scale}}=0$ produces an even steeper slope in the total SME profile at $r_{\text{scale}} < 0.3$.

Finally, the excellent agreement between the direct measurement and our SME model prediction demon-

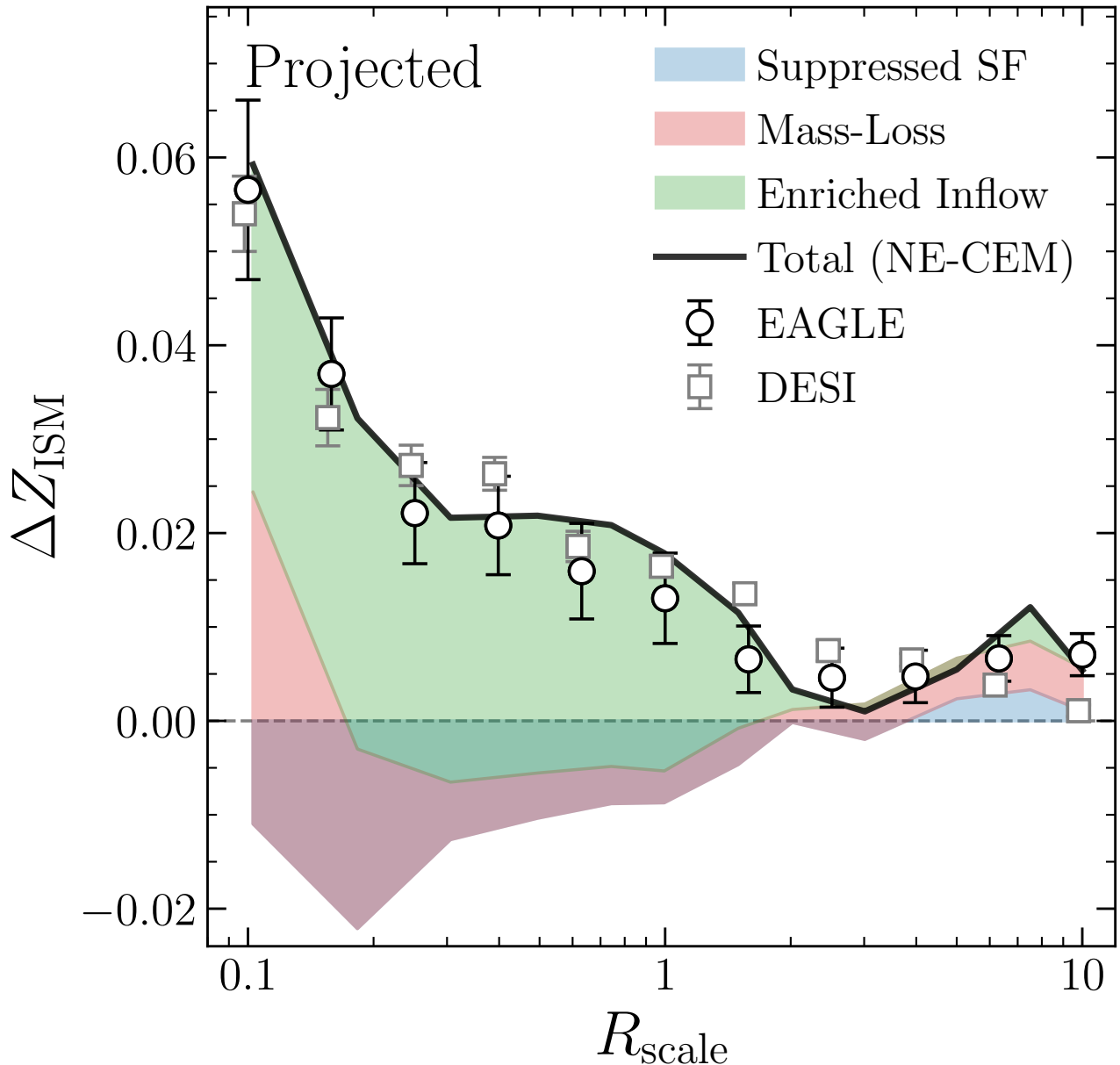


Figure 8. Same as the right panel of Figure 7, but in 2D projected space. Black circles with errorbars are the EAGLE measurement in 2D, while gray squares with errorbars are the overall SME profile measured in DESI DR1. The combination of our physically-motivated decomposition and the satellite NE-CEM model provides an excellent description of the SME profile measured in DESI.

strates that, our satellite NE-CEM is able to capture the key physical processes that drive the SME phenomenon in the EAGLE simulation. We are hopeful that our physically-motivated model will describe, at least qualitatively, the satellites in the real Universe as well, given the similarity of the SME profiles between DESI and EAGLE. To better illustrate how our decomposition can explain the DESI SME profile measured in the projected space, we convert our three SME components from 3D

to 2D using

$$\Delta Z_{\text{ISM}}(R_{\text{scale}}) = \frac{\int_0^{h_{\text{scale}}^{\text{max}}} \Delta Z_{\text{ISM}}(\tilde{r}) n_s(\tilde{r}) dh_{\text{scale}}}{\int_0^{h_{\text{scale}}^{\text{max}}} n_s(\tilde{r}) dh_{\text{scale}}}, \quad (23)$$

where h_{scale} is the line-of-sight distance normalized by halo radius, $h_{\text{scale}}^{\text{max}}$ is the integration limit which we set to 10, n_s is the 3D satellite number density profile around clusters, and $\tilde{r} \equiv \sqrt{R_{\text{scale}}^2 + h_{\text{scale}}^2}$. The results are shown in Figure 8. Open circles and squares with errorbars are the projected SME profiles measured from EAGLE

and DESI (same as those shown in Figure 1), respectively. The blue, red, and green stacks are the 2D projected contributions from suppressed SF, mass-loss, and enriched inflow, respectively. The black solid curve is the sum of the three projected components, providing a good description of the DESI observation.

6. CONCLUSION

In this paper, we present the first measurement of the average SME profile as a function of projected distance (scaled by halo radius) away from galaxy clusters, $\Delta Z_{\text{ISM}}(R_{\text{scale}})$, using the Bright Galaxy Survey galaxies from DESI DR1. The observed SME profile exhibits three distinct regimes: a steep decline with increasing radius at $R_{\text{scale}} < 0.3$, a gradual decrease across the halo boundary over $0.3 < R_{\text{scale}} \leq 2$, and at $R_{\text{scale}} > 2$, a weak but non-zero enhancement extending to $R_{\text{scale}} \sim 10$.

Remarkably, we find that both the shape and amplitude of the DESI SME profile are well reproduced by the EAGLE hydrodynamical simulation at $z=0.1$. This agreement suggests that the subgrid physics implemented in EAGLE likely captures the essential environmental processes regulating chemical enrichment in satellites. Analyzing the EAGLE simulation, we identify three dominant mechanisms that drive the SME around massive clusters: the suppression of star formation experienced by satellite galaxies, the stellar mass loss due to the strong cluster tidal field, and the accretion of enriched gas from the ICM.

Accordingly, we develop a set of clean, controlled experiments to decompose the 3D isotropic EAGLE SME profile $\Delta Z_{\text{ISM}}(r_{\text{scale}})$ into contributions from three physical processes: suppressed star formation, mass loss, and enriched inflow. We find that the suppressed star formation produces a negative SME contribution ($\langle \Delta Z_{\text{ISM}} \rangle \sim -0.02$) with a minimum of $\simeq -0.026$ at $r_{\text{scale}} \simeq 0.3$, likely caused by the “delay-then-rapid” quenching process of satellite galaxies. Meanwhile, mass loss shifts satellite galaxies horizontally on the metallicity vs. stellar mass diagram to the left, thereby producing a (pseudo-) positive SME effect ($\langle \Delta Z_{\text{ISM}} \rangle \sim 0.02$). Having comparable magnitudes but different signs, the contributions from the suppressed star formation and mass loss roughly cancel each other at $0.3 < r_{\text{scale}} < 1$. Within the cluster core at $r_{\text{scale}} \leq 0.3$, however, the two conspire to steepen the increase of the SME profile towards the cluster center.

We find that the enriched inflow dominates the SME in the outer regions of clusters ($0.3 < r_{\text{scale}} < 1$), with a roughly r_{scale} -independent contribution of $\Delta Z_{\text{ISM}} \simeq 0.037$. To better understand the metallicity evolution of satellite galaxies, we develop a satel-

lite NE-CEM that extends the NE-CEM framework of LZ23 to incorporate enriched inflows (i.e., allowing gas accretion to have arbitrary metallicities). Applying our satellite NE-CEM to EAGLE satellites at $r_{\text{scale}} = [0.2, 0.4]$, we successfully recover their average infall time $\tau_{\text{infall}} = 3.34 \pm 0.15$ Gyr and ICM-to-ISM oxygen fraction ratio $f_{\text{inflow}}^{\text{ICM}} = 0.23 \pm 0.02$. Our satellite NE-CEM model reveals that the constant contribution from enriched inflow is due to the rapid elevation of gas-phase metallicities by $(1 - f_{\text{inflow}}^{\text{IGM}})/(1 - f_{\text{inflow}}^{\text{ICM}})$, where $f_{\text{inflow}}^{\text{IGM}} = 0.16$ is the IGM-to-ISM oxygen fraction in EAGLE.

Taken together, our results provide a robust and rigorous physical interpretation of the complex SME profile observed in the DESI data and EAGLE simulation, serving as the foundation for our more comprehensive SME measurements and analyses in papers II and III. In the near future, with upcoming new data releases from DESI, our method will provide increasingly precise constraints on the role of environment in shaping galaxy chemical evolution across the cosmic web. Meanwhile, deeper spectroscopic surveys like the Prime Focus Spectrograph (PFS; M. Takada et al. 2014) will enable SME measurements at higher redshifts than the DESI BGS, while spectroscopic cluster surveys like the Jiaotong University Spectroscopic Telescope (JUST; JUST Team et al. 2024) will reveal an even clearer path of the dynamical and chemical evolution of satellite galaxies as they travel from the infall region to the violent core of clusters.

7. ACKNOWLEDGMENTS

We thank Dirk Scholte, Rita Tojeiro, John Moustakas, Zheng Zheng, and Zhongxu Zhai for their helpful comments and discussions. This work is supported by the National Key Basic Research and Development Program of China (No. 2023YFA1607800, 2023YFA1607804), the National Natural Science Foundation of China (12595313, 12173024), and the China Manned Space Program (No. CMS-CSST-2025-A04). Y.L. is supported by the National Natural Science Foundation of China (123B2040) and the T.D. Lee scholarship. This project is supported in part by Office of Science and Technology, Shanghai Municipal Government (grant Nos. 24DX1400100, ZJ2023-ZD-001). Y.Z. acknowledges the generous sponsorship from Yangyang Development Fund. Y.Z. thanks Cathy Huang for her hospitality at the Zhangjiang High-tech Park.

This material is based upon work supported by the U.S. Department of Energy (DOE), Office of Science, Office of High-Energy Physics, under Contract No. DE-AC02-05CH11231, and by the National Energy Re-

search Scientific Computing Center, a DOE Office of Science User Facility under the same contract. Additional support for DESI was provided by the U.S. National Science Foundation (NSF), Division of Astronomical Sciences under Contract No. AST-0950945 to the NSF's National Optical-Infrared Astronomy Research Laboratory; the Science and Technology Facilities Council of the United Kingdom; the Gordon and Betty Moore Foundation; the Heising-Simons Foundation; the French Alternative Energies and Atomic Energy Commission (CEA); the National Council of Humanities, Science and Technology of Mexico (CONAH-CYT); the Ministry of Science, Innovation and Univer-

sities of Spain (MICIU/AEI/10.13039/501100011033), and by the DESI Member Institutions: <https://www.desi.lbl.gov/collaborating-institutions>. Any opinions, findings, and conclusions or recommendations expressed in this material are those of the author(s) and do not necessarily reflect the views of the U. S. National Science Foundation, the U. S. Department of Energy, or any of the listed funding agencies.

The authors are honored to be permitted to conduct scientific research on I'oligam Du'ag (Kitt Peak), a mountain with particular significance to the Tohono O'odham Nation.

REFERENCES

- Adame, A. G., Aguilar, J., Ahlen, S., et al. 2025, JCAP, 2025, 028, doi: [10.1088/1475-7516/2025/07/028](https://doi.org/10.1088/1475-7516/2025/07/028)
- Andrews, B. H., & Martini, P. 2013, ApJ, 765, 140, doi: [10.1088/0004-637X/765/2/140](https://doi.org/10.1088/0004-637X/765/2/140)
- Baldwin, J. A., Phillips, M. M., & Terlevich, R. 1981, PASP, 93, 5, doi: [10.1086/130766](https://doi.org/10.1086/130766)
- Behroozi, P. S., Wechsler, R. H., & Conroy, C. 2013, ApJ, 770, 57, doi: [10.1088/0004-637X/770/1/57](https://doi.org/10.1088/0004-637X/770/1/57)
- Blanton, M. R., & Moustakas, J. 2009, ARA&A, 47, 159, doi: [10.1146/annurev-astro-082708-101734](https://doi.org/10.1146/annurev-astro-082708-101734)
- Boselli, A., & Gavazzi, G. 2006, PASP, 118, 517, doi: [10.1086/500691](https://doi.org/10.1086/500691)
- Bouché, N., Dekel, A., Genzel, R., et al. 2010, ApJ, 718, 1001, doi: [10.1088/0004-637X/718/2/1001](https://doi.org/10.1088/0004-637X/718/2/1001)
- Brooks, A. M., Governato, F., Quinn, T., Brook, C. B., & Wadsley, J. 2009, ApJ, 694, 396, doi: [10.1088/0004-637X/694/1/396](https://doi.org/10.1088/0004-637X/694/1/396)
- Cardelli, J. A., Clayton, G. C., & Mathis, J. S. 1989, ApJ, 345, 245, doi: [10.1086/167900](https://doi.org/10.1086/167900)
- Chabrier, G. 2003, PASP, 115, 763, doi: [10.1086/376392](https://doi.org/10.1086/376392)
- Cowie, L. L., Songaila, A., Hu, E. M., & Cohen, J. G. 1996, AJ, 112, 839, doi: [10.1086/118058](https://doi.org/10.1086/118058)
- Crain, R. A., Schaye, J., Bower, R. G., et al. 2015, MNRAS, 450, 1937, doi: [10.1093/mnras/stv725](https://doi.org/10.1093/mnras/stv725)
- Curti, M., Mannucci, F., Cresci, G., & Maiolino, R. 2020, MNRAS, 491, 944, doi: [10.1093/mnras/stz2910](https://doi.org/10.1093/mnras/stz2910)
- Curti, M., D'Eugenio, F., Carniani, S., et al. 2023, MNRAS, 518, 425, doi: [10.1093/mnras/stac2737](https://doi.org/10.1093/mnras/stac2737)
- Davé, R., Finlator, K., & Oppenheimer, B. D. 2012, MNRAS, 421, 98, doi: [10.1111/j.1365-2966.2011.20148.x](https://doi.org/10.1111/j.1365-2966.2011.20148.x)
- De Rossi, M. E., Bower, R. G., Font, A. S., Schaye, J., & Theuns, T. 2017, MNRAS, 472, 3354, doi: [10.1093/mnras/stx2158](https://doi.org/10.1093/mnras/stx2158)
- DESI Collaboration, Aghamousa, A., Aguilar, J., et al. 2016a, arXiv e-prints, arXiv:1611.00036, doi: [10.48550/arXiv.1611.00036](https://doi.org/10.48550/arXiv.1611.00036)
- DESI Collaboration, Aghamousa, A., Aguilar, J., et al. 2016b, arXiv e-prints, arXiv:1611.00037, doi: [10.48550/arXiv.1611.00037](https://doi.org/10.48550/arXiv.1611.00037)
- DESI Collaboration, Abareshi, B., Aguilar, J., et al. 2022, AJ, 164, 207, doi: [10.3847/1538-3881/ac882b](https://doi.org/10.3847/1538-3881/ac882b)
- DESI Collaboration, Adame, A. G., Aguilar, J., et al. 2024a, AJ, 167, 62, doi: [10.3847/1538-3881/ad0b08](https://doi.org/10.3847/1538-3881/ad0b08)
- DESI Collaboration, Adame, A. G., Aguilar, J., et al. 2024b, AJ, 168, 58, doi: [10.3847/1538-3881/ad3217](https://doi.org/10.3847/1538-3881/ad3217)
- DESI Collaboration, Abdul-Karim, M., Adame, A. G., et al. 2025, arXiv e-prints, arXiv:2503.14745, doi: [10.48550/arXiv.2503.14745](https://doi.org/10.48550/arXiv.2503.14745)
- Dey, A., Schlegel, D. J., Lang, D., et al. 2019, AJ, 157, 168, doi: [10.3847/1538-3881/ab089d](https://doi.org/10.3847/1538-3881/ab089d)
- Ellison, S. L., Simard, L., Cowan, N. B., et al. 2009, MNRAS, 396, 1257, doi: [10.1111/j.1365-2966.2009.14817.x](https://doi.org/10.1111/j.1365-2966.2009.14817.x)
- Erb, D. K., Shapley, A. E., Pettini, M., et al. 2006, ApJ, 644, 813, doi: [10.1086/503623](https://doi.org/10.1086/503623)
- Finlator, K., & Davé, R. 2008, MNRAS, 385, 2181, doi: [10.1111/j.1365-2966.2008.12991.x](https://doi.org/10.1111/j.1365-2966.2008.12991.x)
- Fujita, Y. 2004, PASJ, 56, 29, doi: [10.1093/pasj/56.1.29](https://doi.org/10.1093/pasj/56.1.29)
- Furlong, M., Bower, R. G., Theuns, T., et al. 2015, MNRAS, 450, 4486, doi: [10.1093/mnras/stv852](https://doi.org/10.1093/mnras/stv852)
- Green, S. B., van den Bosch, F. C., & Jiang, F. 2021, MNRAS, 503, 4075, doi: [10.1093/mnras/stab696](https://doi.org/10.1093/mnras/stab696)
- Gupta, A., Yuan, T., Torrey, P., et al. 2018, MNRAS, 477, L35, doi: [10.1093/mnrasl/sly037](https://doi.org/10.1093/mnrasl/sly037)
- Guy, J., Bailey, S., Kremin, A., et al. 2023, AJ, 165, 144, doi: [10.3847/1538-3881/acb212](https://doi.org/10.3847/1538-3881/acb212)

- Hahn, C., Wilson, M. J., Ruiz-Macias, O., et al. 2023, *AJ*, 165, 253, doi: [10.3847/1538-3881/accff8](https://doi.org/10.3847/1538-3881/accff8)
- JUST Team, Liu, C., Zu, Y., et al. 2024, *Astronomical Techniques and Instruments*, 1, 16, doi: [10.61977/ati2024008](https://doi.org/10.61977/ati2024008)
- Kauffmann, G., Heckman, T. M., White, S. D. M., et al. 2003, *MNRAS*, 341, 33, doi: [10.1046/j.1365-8711.2003.06291.x](https://doi.org/10.1046/j.1365-8711.2003.06291.x)
- Kennicutt, Jr., R. C. 1998, *ApJ*, 498, 541, doi: [10.1086/305588](https://doi.org/10.1086/305588)
- Lara-López, M. A., Cepa, J., Bongiovanni, A., et al. 2010, *A&A*, 521, L53, doi: [10.1051/0004-6361/201014803](https://doi.org/10.1051/0004-6361/201014803)
- Larson, R. B., Tinsley, B. M., & Caldwell, C. N. 1980, *ApJ*, 237, 692, doi: [10.1086/157917](https://doi.org/10.1086/157917)
- Lequeux, J., Peimbert, M., Rayo, J. F., Serrano, A., & Torres-Peimbert, S. 1979, *A&A*, 80, 155
- Levi, M., Bebek, C., Beers, T., et al. 2013, arXiv e-prints, arXiv:1308.0847, doi: [10.48550/arXiv.1308.0847](https://doi.org/10.48550/arXiv.1308.0847)
- Lilly, S. J., Carollo, C. M., Pipino, A., Renzini, A., & Peng, Y. 2013, *ApJ*, 772, 119, doi: [10.1088/0004-637X/772/2/119](https://doi.org/10.1088/0004-637X/772/2/119)
- Lin, Y., & Zu, Y. 2023, *MNRAS*, 521, 411, doi: [10.1093/mnras/stad502](https://doi.org/10.1093/mnras/stad502)
- Maier, C., Ziegler, B. L., Haines, C. P., & Smith, G. P. 2019, *A&A*, 621, A131, doi: [10.1051/0004-6361/201834290](https://doi.org/10.1051/0004-6361/201834290)
- Mannucci, F., Cresci, G., Maiolino, R., Marconi, A., & Gnerucci, A. 2010, *MNRAS*, 408, 2115, doi: [10.1111/j.1365-2966.2010.17291.x](https://doi.org/10.1111/j.1365-2966.2010.17291.x)
- Mannucci, F., Cresci, G., Maiolino, R., et al. 2009, *MNRAS*, 398, 1915, doi: [10.1111/j.1365-2966.2009.15185.x](https://doi.org/10.1111/j.1365-2966.2009.15185.x)
- Manuwal, A., & Stevens, A. R. H. 2023, *MNRAS*, 523, 2738, doi: [10.1093/mnras/stad1587](https://doi.org/10.1093/mnras/stad1587)
- Moore, B., Katz, N., Lake, G., Dressler, A., & Oemler, A. 1996, *Nature*, 379, 613, doi: [10.1038/379613a0](https://doi.org/10.1038/379613a0)
- Mouhcine, M., Baldry, I. K., & Bamford, S. P. 2007, *MNRAS*, 382, 801, doi: [10.1111/j.1365-2966.2007.12405.x](https://doi.org/10.1111/j.1365-2966.2007.12405.x)
- Moustakas, J., Buhler, J., Scholte, D., Dey, B., & Khederlarian, A. 2023, *FastSpecFit: Fast spectral synthesis and emission-line fitting of DESI spectra*, Astrophysics Source Code Library, record ascl:2308.005 <http://ascl.net/2308.005>
- Pasquali, A., Gallazzi, A., & van den Bosch, F. C. 2012, *MNRAS*, 425, 273, doi: [10.1111/j.1365-2966.2012.21454.x](https://doi.org/10.1111/j.1365-2966.2012.21454.x)
- Peng, Y., Maiolino, R., & Cochrane, R. 2015, *Nature*, 521, 192, doi: [10.1038/nature14439](https://doi.org/10.1038/nature14439)
- Peng, Y.-j., & Maiolino, R. 2014, *MNRAS*, 438, 262, doi: [10.1093/mnras/stt2175](https://doi.org/10.1093/mnras/stt2175)
- Petropoulou, V., Vílchez, J., Iglesias-Páramo, J., et al. 2011, *ApJ*, 734, 32, doi: [10.1088/0004-637X/734/1/32](https://doi.org/10.1088/0004-637X/734/1/32)
- Planck Collaboration, Aghanim, N., Akrami, Y., et al. 2020, *A&A*, 641, A6, doi: [10.1051/0004-6361/201833910](https://doi.org/10.1051/0004-6361/201833910)
- Poppett, C., Tyas, L., Aguilar, J., et al. 2024, *AJ*, 168, 245, doi: [10.3847/1538-3881/ad76a4](https://doi.org/10.3847/1538-3881/ad76a4)
- Sanders, R. L., Shapley, A. E., Jones, T., et al. 2021, *ApJ*, 914, 19, doi: [10.3847/1538-4357/abf4c1](https://doi.org/10.3847/1538-4357/abf4c1)
- Savaglio, S., Glazebrook, K., Le Borgne, D., et al. 2005, *ApJ*, 635, 260, doi: [10.1086/497331](https://doi.org/10.1086/497331)
- Schaye, J., Crain, R. A., Bower, R. G., et al. 2015, *MNRAS*, 446, 521, doi: [10.1093/mnras/stu2058](https://doi.org/10.1093/mnras/stu2058)
- Schindler, S., Kapferer, W., Domainko, W., et al. 2005, *A&A*, 435, L25, doi: [10.1051/0004-6361:200500107](https://doi.org/10.1051/0004-6361:200500107)
- Schlafly, E. F., Kirkby, D., Schlegel, D. J., et al. 2023, *AJ*, 166, 259, doi: [10.3847/1538-3881/ad0832](https://doi.org/10.3847/1538-3881/ad0832)
- Shields, G. A., Skillman, E. D., & Kennicutt, Jr., R. C. 1991, *ApJ*, 371, 82, doi: [10.1086/169872](https://doi.org/10.1086/169872)
- Skillman, E. D., Kennicutt, Jr., R. C., Shields, G. A., & Zaritsky, D. 1996, *ApJ*, 462, 147, doi: [10.1086/177138](https://doi.org/10.1086/177138)
- Sotillo-Ramos, D., Lara-López, M. A., Pérez-García, A. M., et al. 2021, *MNRAS*, 508, 1817, doi: [10.1093/mnras/stab2641](https://doi.org/10.1093/mnras/stab2641)
- Takada, M., Ellis, R. S., Chiba, M., et al. 2014, *PASJ*, 66, R1, doi: [10.1093/pasj/pst019](https://doi.org/10.1093/pasj/pst019)
- Taylor, J. E., & Babul, A. 2004, *MNRAS*, 348, 811, doi: [10.1111/j.1365-2966.2004.07395.x](https://doi.org/10.1111/j.1365-2966.2004.07395.x)
- Topping, M. W., Shapley, A. E., Sanders, R. L., et al. 2021, *MNRAS*, 506, 1237, doi: [10.1093/mnras/stab1793](https://doi.org/10.1093/mnras/stab1793)
- Tremonti, C. A., Heckman, T. M., Kauffmann, G., et al. 2004, *ApJ*, 613, 898, doi: [10.1086/423264](https://doi.org/10.1086/423264)
- Wang, X., Jones, T. A., Treu, T., et al. 2019, *ApJ*, 882, 94, doi: [10.3847/1538-4357/ab3861](https://doi.org/10.3847/1538-4357/ab3861)
- Weinberg, D. H., Andrews, B. H., & Freudenburg, J. 2017, *ApJ*, 837, 183, doi: [10.3847/1538-4357/837/2/183](https://doi.org/10.3847/1538-4357/837/2/183)
- Wetzel, A. R., Tinker, J. L., Conroy, C., & van den Bosch, F. C. 2013, *MNRAS*, 432, 336, doi: [10.1093/mnras/stt469](https://doi.org/10.1093/mnras/stt469)
- Williamson, D., Martel, H., & Romeo, A. B. 2016, *ApJ*, 831, 1, doi: [10.3847/0004-637X/831/1/1](https://doi.org/10.3847/0004-637X/831/1/1)
- Yang, X., Xu, H., He, M., et al. 2021, *ApJ*, 909, 143, doi: [10.3847/1538-4357/abddb2](https://doi.org/10.3847/1538-4357/abddb2)
- York, D. G., Adelman, J., Anderson, Jr., J. E., et al. 2000, *AJ*, 120, 1579, doi: [10.1086/301513](https://doi.org/10.1086/301513)
- Zabludoff, A. I., & Mulchaey, J. S. 1998, *ApJ*, 496, 39, doi: [10.1086/305355](https://doi.org/10.1086/305355)
- Zaritsky, D., Kennicutt, Jr., R. C., & Huchra, J. P. 1994, *ApJ*, 420, 87, doi: [10.1086/173544](https://doi.org/10.1086/173544)